Study of Wall Slip in Entangled Polymer Melts Using Stochastic Simulation

By

Fang Xu

A Dissertation Submitted to the Graduate Faculty in Engineering in Partial Fulfillment of the Requirements for the Degree of Doctor of Philosophy

The City University of New York
2006

ProQuest Information and Learning Company
300 North Zeeb Road
P.O. Box 1346
Ann Arbor, MI 48106-1346

This manuscript has been read and accepted for the
Graduate Faculty in Engineering in satisfaction of the
dissertation requirement for the degree of Doctor of Philosophy.

Morton M. Denn

Date — Chair of Examining Committee

Mumtaz K. Kassir

Date — Executive Officer

Alexander Couzis

Christopher Durning

Joel Koplik

Raymond Tu

Supervisory Committee

THE CITY UNIVERSITY OF NEW YORK

Abstract

Study of Wall Slip in Entangled Polymer Melts Using Stochastic Simulation

By

Fang Xu

Advisor: Professor Morton M. Denn

We describe a full-chain stochastic tube model for entangled melts and solutions of linear polymers. The model incorporates two forces that result from chain confinement: a tensile force along the chain that prevents chain collapse and a transverse force that keeps the chain within the virtual tube. The model tracks conjugate constraint pairs and utilizes a consistent approach to constraint release and renewal. Chain loops within the tube are permitted. A single time-scaling adjustable parameter is required. Model predictions are compared with published transient and steady-state data on two entangled polystyrene solutions.

The stochastic chain model described above provides fundamental insight into the mechanism of apparent wall slip in entangled polymer melts. Apparent slip is a shown to be a consequence of a rapid decrease in the entanglement density for chains in the region of the wall. There is good agreement between model predictions and polydimethylsiloxane experiments of Durliat *et al*. (1997) in which a surface layer containing a known density of tethered chains contacts a bulk melt. The model cannot

provide quantitative information about apparent slip when chains are simply adsorbed at the wall, since the surface density and effective chain length are required inputs to the calculation, but it does agree in broad terms with experiments of Mhetar and Archer (1998a) on 1,4-polybutadiene.

Acknowledgements

I wish to express my most sincere gratitude to my advisor, Professor Morton M. Denn, for his patient guidance and continual encouragement throughout the course of my Ph.D.

I would like to thank Professor Jay D. Schieber for his valuable discussions and suggestions.

Many thanks to Andy Eng, Igor, Junjun, Zhen Rong Xu and Mary for their technical support.

I also would like to thank my family for their love and support. This work is especially dedicated to my husband, Bo, and my son, Eric, who made it all worthwhile.

Contents

List of Tables

List of Figures

List of flowcharts

Chapter 1

A full-chain stochastic tube model for entangled melts and solutions of linear polymers

1.1 Introduction

Tube models for the dynamics of highly entangled polymer melts and concentrated solutions generalize the original reptation model of Doi and Edwards(1978a; b; c; 1979; 1986). The polymer chain is assumed to move in a "tube" formed by the topological constraints imposed by surrounding chains. Doi and Edwards made the following assumptions about the chain and the tube: (i) the primitive chain length is constant; (ii) the chain has no connectivity; (iii) the tube is a static object and its velocity is neglected; and (iv) the constraints formed by the surrounding chains are fixed. These four assumptions have been relaxed in numerous subsequent modifications, with notable contributions by Doi(1983) (segment connectivity); Pearson, Marrucci, and Grizzuti (1991) (tube stretching); Ianniruberto and Marrucci (1996) (convective constraint release); and Mead, Larson and Doi (1998) (chain length fluctuations and convective constraint release). Tube models have been reviewed by McLeish (2002).

Hua and Schieber (1998a; b; 1999) proposed an approach to tube models that integrates segment connectivity, chain-length breathing, segmental stretch, and constraint release in a full-chain stochastic simulation. A polymer chain, which is represented by a series of friction points ("beads") connected by finitely extensible nonlinear (*FENE*)

springs, is confined within a tube. The force balance on each bead includes the frictional force, the spring restoring force, and a Brownian force; an excluded volume constraint prevents beads from passing one another in the tube. The tube, which is described by a finite set of independent connectors representing entanglements, is convected and deformed affinely by the flow. The tube length changes with the length of the chain; a new tube segment is created when an end of the chain moves out of the existing tube, while a constraint is released when a tube segment is destroyed by retraction of the chain. A Kramers-type expression is used to calculate the stress that is contributed by the polymer chain. This stochastic chain model successfully captures the experimental trends for simple shear flow, single-step-strain flow, double-step-strain flow, and exponential shear flow.

The model as formulated by Hua and Schieber has three limitations, however. The excluded volume constraint ensures that a chain cannot collapse in the tube, but it prevents the formation of explicit chain loops within the tube. The algorithm does not call for the creation of a new constraint on another chain in the ensemble when a new tube segment is added at the end of a chain, so the kinetics of constraint release and constraint formation are unbalanced. Finally, the computed stress depends on the number of beads used in coarse-graining the chain; this computational anomaly is a consequence of the use of a one-dimensional projection of the chain within the tube.

We describe in this chapter a stochastic tube model in which the excluded volume constraint is removed and chain loops are permitted, the constraint release and formation kinetics are consistent, and the computed response is independent of the degree of coarse-graining.

1.2 Model description

Each polymer molecule in the ensemble is modeled as a series of N beads connected by N–1 springs; the chain is confined to the region of a three-dimensional primitive path by an axisymmetric harmonic tube potential. The primitive path is formed by Z segments that have different orientations and lengths, as shown schematically in Fig. 1. A vector $\boldsymbol{U}_t$ represents tube segment t, $1 \le t \le Z$; the unit vector $\boldsymbol{u}_t$ is defined as $\boldsymbol{U}_t / |\boldsymbol{U}_t|$. $\boldsymbol{R}_\mathbf{i}$ denotes the position of the i-th bead along the chain relative to the beginning of the segment in which the bead is located, $1 \le i \le N$. The configuration of the tube changes with the surrounding flow field, while the length changes with the length of the confined chain. Because of constraint release and constraint creation, neither the spacing nor the number of strands along the chain is constant.

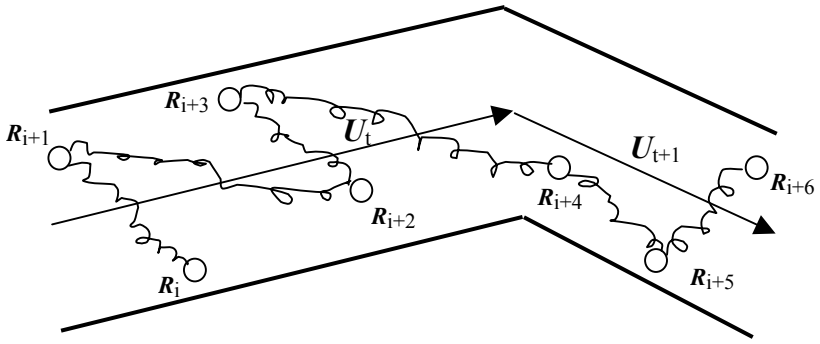

Fig. 1. Sketch of a part of the confined chain in two consecutive tube segments.

Chain confinement causes two forces, a tensile force along the chain that prevents chain collapse and a transverse force that keeps the chain within the virtual tube. The dynamics of the chain are governed by these two forces, together with the spring force, a

viscous drag force, and the Brownian force. Assuming that bead inertia can be neglected, the Langevin equation for each bead is then

$$
\begin{aligned}
0 &= -\zeta\left[\dot{\boldsymbol{R}}_1 - \boldsymbol{v}_{\mathrm{t},1}\right] + \boldsymbol{F}_1^{\mathrm{s}} + \boldsymbol{F}_1^{\mathrm{R}} - \boldsymbol{F}^{\mathrm{T}} + \boldsymbol{F}_1^{\mathrm{B}} \\
0 &= -\zeta\left[\dot{\boldsymbol{R}}_{\mathrm{i}} - \boldsymbol{v}_{\mathrm{t,i}}\right] + \boldsymbol{F}_{\mathrm{i}}^{\mathrm{s}} - \boldsymbol{F}_{\mathrm{i-1}}^{\mathrm{s}} + \boldsymbol{F}_{\mathrm{i}}^{\mathrm{R}} + \boldsymbol{F}_{\mathrm{i}}^{\mathrm{B}}, \mathrm{i} = 2,...,\mathrm{N}-1 \\
0 &= -\zeta\left[\dot{\boldsymbol{R}}_{\mathrm{N}} - \boldsymbol{v}_{\mathrm{t,N}}\right] - \boldsymbol{F}_{\mathrm{N-1}}^{\mathrm{s}} + \boldsymbol{F}_{\mathrm{N}}^{\mathrm{R}} + \boldsymbol{F}^{\mathrm{T}} + \boldsymbol{F}_{\mathrm{N}}{}^{\mathrm{B}}
\end{aligned}
\tag{1}
$$

The first term on the right-hand side of the Langevin equation is the frictional drag resulting from the relative motion of the bead and the tube segment. ζ is a friction coefficient, which is assumed to be the same for all beads; $\boldsymbol{v}_{t,i} = \boldsymbol{\kappa} \cdot \boldsymbol{R}_i$ is the velocity of the tube segment that contains bead *i*, where $\boldsymbol{\kappa}$ is the transpose of the macroscopic velocity gradient. Superscripts *s, R, T,* and *B* on the force terms denote spring, transverse, tensile, and Brownian, respectively.

1.2.1 spring force

As is well known, the finitely extensible nonlinear elastic (FENE) spring is a successful spring model for describing flexible polymers such as polystyrene. The corresponding force law is expressed as

$$
\boldsymbol{F}_i^s \equiv \frac{H(\boldsymbol{R}_{i+1} - \boldsymbol{R}_i)}{1 - (\boldsymbol{R}_{i+1} - \boldsymbol{R}_i)^2 / b^2} \tag{2}
$$

for the spring force between the $(i+1)^{th}$ and i^{th} beads, with the spring constant $H = \frac{3k_B T(N-1)}{N_k a_k^{\,2}}$ and the extensibility $b = \frac{N_k a_k}{N-1}$; here, k_B is Boltzmann constant, T is the temperature, a_k denotes the Kuhn length (the correlation length of the chain) and N_k is the number of Kuhn lengths in the chain. Values of the Kuhn lengths for common polymers are summarized by Flory (1969), Volkenstein (1963), and Birshtein (1966). (Equation (2) is written for the case in which both beads i and i+1 are in the same tube segment. The position vectors are referred to a common origin in calculating the spring force if the beads are in adjacent segments.)

1.2.2 Brownian force

In our molecular level model, thermal fluctuations play an important role in determining the motion of polymer chains. Therefore, it is necessary to introduce a Brownian force into the governing equations. Here, we assume that the Brownian motions of each bead due to thermal fluctuations are independent. The strength of the Brownian force is determined from the principle of equipartition of energy; that is, the equilibrium kinetic energy of the Brownian particle should be $\frac{1}{2}k_B T$, which gives a relationship between the friction and Brownian forces. This relationship is also known as the fluctuation – dissipation theorem. Furthermore, since the Brownian forces are caused by many independent collisions, the central limit theorem suggests that the Brownian force is a Gaussian process. Thus, the Brownian force $\boldsymbol{F}^B$ can be represented by

$$\sqrt{2k_B T\zeta}\, d\boldsymbol{W}(t) \;/ dt\,, \qquad (3)$$

where $\boldsymbol{W}(t)$ is a Weiner process satisfying $<\boldsymbol{W}(t)> =0$ and $<\boldsymbol{W}(t_1)\boldsymbol{W}(t_2)>=\min(t_1,t_2)$ (Ottinger, 1996).

1.2.3 Tensile force

As mentioned earlier, the chain, whose motion in the direction perpendicular to the tube is constrained, experiences an osmotic like effect from the wall of the tube. A tensile force acting along the tube direction is thus introduced due to this effect; this force also ensures that a chain moving within the network remains a random walk. The resulting tensile force is

$$F^T = 3k_B T\sqrt{Z / N_k a_k^2} \tag{4}$$

where Z is the tube entanglement number and consequently $\sqrt{N_k a_k^2 / Z}$ is the average segment length. The derivation of Eq. (4) is shown in Appendix A. The tensile force replaces the excluded volume constraint contained in the Hua and Schieber model.

1.2.4 Transverse force

The position vector $\boldsymbol{R}_i$ can be decomposed into components parallel and orthogonal to the tube segment direction,

$$\boldsymbol{R}_i = s_i \boldsymbol{u}_{t(i)} + \boldsymbol{P}_i , \tag{5}$$

where subscript t(i) denotes the index of the tube segment in which i^{th} bead is located and

$$s_i = \boldsymbol{R}_i \cdot \boldsymbol{u}_{t(i)} . \tag{6}$$

The transverse force will depend on the transverse displacement. The force keeps the bead away from the tube "wall" and, with an assumption of axisymmetry, should lead to a most probable position at the center of the tube at equilibrium. Hence, to a lowest-order approximation, the transverse force may be taken to be proportional $-\boldsymbol{P}_i$. The force is derived in Appendix B as

$$\boldsymbol{F}_i^R = -\alpha_i \boldsymbol{P}_i , \tag{7}$$

$$\alpha_i = \begin{cases} -\dfrac{2(K-1)}{K} H & i = 1, N \\ (-4 - \dfrac{2}{K-2} + \dfrac{2}{K}) H & i \neq 1, N \end{cases} \tag{8}$$

Here, $K = 1 - \dfrac{3Z}{2(N-1)}$. This harmonic force, which guarantees that the chain remains a random walk on all length scales, is not contained in the Hua and Schieber model, and its inclusion is necessary for the results to be independent of the number of beads used for coarse-graining. Since we expect that K > 0, the number of beads should be greater than 1 + 3Z/2. The transverse force seems to be similar in concept to the "interchain pressure" of Marrucci and Ianniruberto (2004), but the analytical forms differ. Although Eq. (8) is derived only for flows for which the product of the shear rate with $\zeta/4H$ is much less than unity, we use it for flows of all magnitudes. We show subsequently that this assumption is self-consistent.

From Eq. (B16) we can readily show that the equilibrium value for $< \left| \boldsymbol{P}_i \boldsymbol{P}_i \right| >$ is

$$< \left| \boldsymbol{P}_i \boldsymbol{P}_i \right| >= \frac{(2N - 2 + 3Z_{eq})(2N - 2 - 3Z_{eq})}{12Z_{eq}(N-1)} \frac{N_K a_K^2}{3(N-1)} \tag{9}$$

where $\sqrt{N_k a_k^2 / Z}_{eq}$ is the tube segment length at equilibrium (Doi and Edwards, 1986). Hence, if we interpret $2\sqrt{< \left| \boldsymbol{P}_i \boldsymbol{P}_i \right| >}$ to be the effective diameter of the "tube" at equilibrium, it follows that the limiting value for the tube diameter as N $\rightarrow \infty$ is equal to 2/3 the mean entanglement spacing.

1.2.5 Tube deformation

In our model, the tube is allowed to be deformed by the flow field, and the affine deformation of the tube segment from time t' to t is described by

$$\boldsymbol{U}_t(\mathrm{t}) = \exp\left[\int_{t'}^{t} \boldsymbol{\kappa}(\mathrm{t}'')\boldsymbol{d}\,\mathrm{t}'' \right] \cdot \boldsymbol{U}_t(\mathrm{t}'). \tag{10}$$

$\lceil \ \rceil$ indicates a time-ordering operator (Van Kampen, 1992).

1.2.6 Stress tensor

In polymer melts or highly concentrated polymer solutions, the stress is mainly contributed by the polymer, and viscous stress from the solvent is usually neglected. During our stochastic simulation, we track the locations of each bead as well as that of

each tube segment. To convert such information into properties comparable to the experimental measurements, we need a suitable formula for the calculation of stress tensor. In our model, we choose the Kramers formula (Bird, Armstrong *et al.*, 1987),

$$\boldsymbol{\tau}^{p} = \sum_{i=1}^{N-1} < \boldsymbol{F}_i^{s} (\boldsymbol{R}_{i+1} - \boldsymbol{R}_i) > - \sum_{i=1}^{N-1} \left| \boldsymbol{F}^{T} \right| < (s_{i+1} - s_i) \boldsymbol{u}_i \boldsymbol{u}_i > - \sum_{i=1}^{N} \alpha_i < \boldsymbol{P}_i \boldsymbol{P}_i > + nk_B T \boldsymbol{\delta} \quad (11)$$

where the non-isotropic terms of $\boldsymbol{\tau}^{p}$ come from the spring force, tension force and repulsive force, The last term arises from the momentum of the chain, sometimes referred to as the Brownian motion contribution. The tensile force contribution contains an assumption that the first bead in each segment is at the beginning of the segment in order to obtain an explicit form; this assumption is increasingly better as the ratio N/Z increases, and the stress expression is exact in the limits of infinite N/Z and Z = 1 for any N.

1.2.7 Model parameters

The model contains only three parameters: the number of beads, *N*; the friction coefficient for each bead, ζ; and the number of segments at equilibrium, $<Z>_{eq}$. All other model inputs are determined by the composition of the polymer chain. The results must be independent of the coarse-graining parameter N, and we show subsequently that this is the case. The other two parameters would typically be set by comparison of simulations to data, usually to data that are defined by the reptation time and the plateau modulus. We have done calculations in which $<Z>_{eq}$ is treated as an adjustable parameter, but we have found that it suffices to adopt the method used by Hua & Schieber (1998) to estimate the equilibrium number of segments, namely

$$<Z>_{eq} \approx \varphi^{x} M_w/M_e, \tag{12}$$

where φ is the volume fraction of polymer, M_w is the molecular weight, and M_e is the molecular weight between entanglements, which is assumed to be independently available. The exponent x depends on solvent quality and is taken as 1.2 for the polystyrene solutions described subsequently. [The value 1.2 is typically used by the Illinois Institute of Technology group for polystyrene in good solvents (e.g., (Venerus and Nair, 2006), although values as low as 1.0 have been observed. Rubinstein and Colby (2003) give a value of 1.3 for a number of polymer-solvent pairs.] Hence, the friction coefficient ζ is the only parameter that is not known *a priori*.

The calculations are carried out in dimensionless form, with length, time, and stress made dimensionless by $\sqrt{k_B T / H}$, $\lambda_{\boldsymbol{H}} \equiv \zeta / 4H$, and nk_BT, respectively, where n is the number density of polymer chains. λ_H is equal to the Rouse time divided by $4N(N-1)/\pi^2$. The value of ζ (or λ_H) is required only to obtain the absolute time scale for comparison with experiments.

1.2.8 Constraint release and formation

The simulation is started at equilibrium, where the tube segment length is $\sqrt{N_k a_k^2 / < Z >_{eq}}$. We assume that all entanglements are between two different chains, and we randomly assign pairs. Hence, the entire entanglement distribution is known initially, and the pairing is tracked throughout the simulation.

The tube shape is updated for each time step according to Eq. 10, and chain dynamics are computed using a first-order Euler forward difference scheme that is described in Appendix C. The lengths of the end tube segments are adjusted to correspond to the positions of the first and last beads in the tube (which may not be the first and last beads on the chain because of the possibility of end loops). Any time that a chain retracts sufficiently far into the tube to leave the final tube segment empty, the segment is removed and a constraint is released. The conjugate constraint on another chain is released at the same time, and the adjacent tube segments are combined into one. The tube length is shortened when the conjugate entanglement is released, since a straight segment replaces two segments that meet at an angle.

If a chain reptates out of the tube and the end tube segment is less than the equilibrium value, the tube segment is extended to incorporate the chain. If a chain reptates out of a tube that is already equal to the equilibrium segment length, a new tube segment is formed in a random direction, corresponding to a new constraint. A tube segment in the ensemble is then selected randomly; if the length of that tube segment is larger than the equilibrium segment length, a new conjugate constraint is created at the midpoint of that segment, with the segment junction displaced in a random direction from the position of the prior single segment. The amount of the displacement is chosen to make the increase in the total length of each tube in the ensemble equal to the decrease in the sum of all tube lengths in the ensemble resulting from the removal of constraints during the same time step divided by the number of removed constraints. The positions of new constraint pairs are recorded and tracked during the simulation.

The algorithm for constraint release is different from that of Hua and Schieber (1998), which does not track conjugate constraint pairs. There is no mechanism in their algorithm for creating constraints at internal segments, so constraints concentrate at the tube ends.

The details of the simulation procedures are described in Appendix D.

1.3 Results

1.3.1 Experiments of Venerus and Kahvand.

Venerus and Kahvand (1994; Kahvand, 1995) studied a 13 volume % tricresyl phosphate solution of polystyrene with a molecular weight of 1.9×10^6 and a polydispersity of 1.2. This fluid had a zero-shear viscosity $\eta_0 = 6.8\times10^3$ Pa·s and a zero-shear first normal stress coefficient $\psi_{1,0} = 2.0\times10^5$ Pa·s^2; the mean relaxation time $\tau_d = \psi_{1,0}/2\eta_0 = 14.7$ s. The molecular weight between entanglement points is approximately 1.8×10^4 (Ferry, 1980), hence the equilibrium number of segments $\langle Z\rangle_{eq}$ from Eq. 12 is around 9. N is taken equal to $4\langle Z\rangle_{eq} + 1$ in the calculations shown in this section. The invariance of the results with respect to N is demonstrated subsequently.

The magnitude of λ_H was estimated from the steady zero-shear data using a computed linear relaxation modulus. First, the relaxation modulus was simulated using a Green-Kubo linear response equation:

$$G(t) = \frac{1}{nk_BT\Lambda}\int_0^{\Lambda} < \tau_{xy}(t')\tau_{xy}(t'+t) >_{eq}\, dt' \qquad (13)$$

Λ is the averaging interval, which is increased until convergence is obtained. (The convergence with Λ is shown in Appendix E.) The simulation was then fitted with three Maxwell modes (shown in Table 1 using Origin 7.0 software, whose nonlinear regression method is based on the Levenberg-Marquardt (LM) algorithm), in the form $G(t)/nk_BT = \sum g_j \exp(-t/\lambda_j)$, as shown in Fig. 2a, and λ_H was obtained as $\lambda_H = 2.34\times10^{-3}$ s, corresponding to a Rouse time of 1.27 s, from the experimental value of $\psi_{i,o}/\eta_o = \sum g_i\lambda_i^2/\sum g_i\lambda_i$. [The fitting could have been done to the individual values of either η_o or $\psi_{i,o}$, to any other single experimental value that can be computed from G(t), or to a characteristic time in a transient experiment. The Rouse time is 0.81 s if λ_H is calculated from the experimental zero-shear viscosity, and 1.01 s if λ_H is calculated from the experimental zero-shear normal stress coefficient.] The simulated relaxation moduli with different time steps and bead numbers are shown in Appendices F and G, respectively. The predicted linear viscoelastic properties G' and G" are shown in Fig. 2b, together with the experimental data. The fit is very good in the terminal region, the neighborhood of the crossover frequency, and the region of the plateau modulus; the deviation in G" at frequencies above $2s^{-1}$ is a consequence of the coarse graining inherent in tube models and the three-term fit, which cannot capture the shortest time constants. In Appendix F, we can see that the prediction for the high frequency is improved with the increased bead numbers. (The intrinsic coarse graining limit for $N \rightarrow \infty$ is likely to be of the order of the Rouse time of a chain equal to the length contained in a tube segment, which will be of the order of the Rouse time of the entire chain divided by Z^2. This would correspond to a frequency of about $60s^{-1}$ for these data.) The Cox-Merz rule is shown to be valid in Appendix H.

Table 1 Fitted discrete relaxation spectrum for Venerus and Kahvand's data

Weight factor g_i/nk_BT	Standard error	Time constant $\lambda_i/1878.6\lambda_H$	Standard error
2.398	±0.077	4.107	±0.049
4.019	±0.019	0.162	±0.002
1.833	±0.067	1.679	±0.051

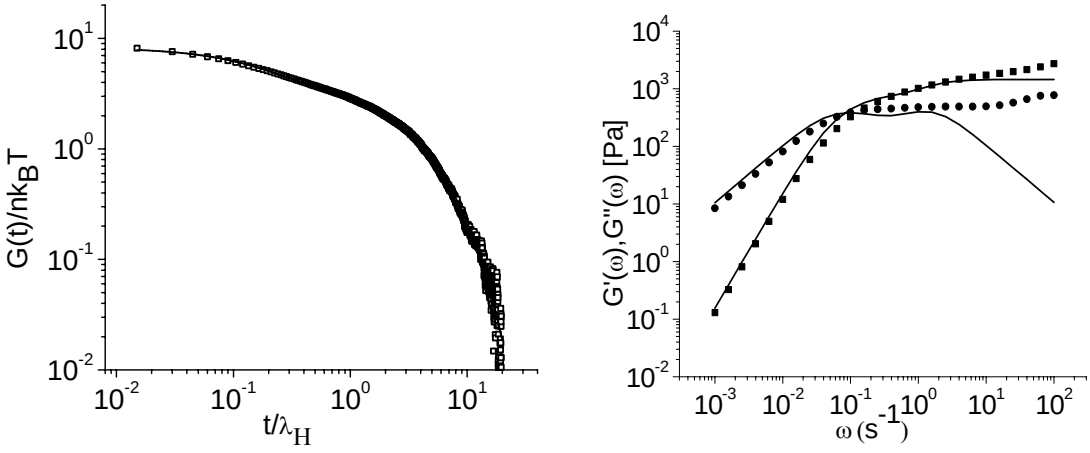

(a) (b)

Fig. 2. (a) G(t) computed from the Green-Kubo equation. The line is the three-term fit. (b) G' (■) and G" (●) data of Venerus and Kahvand. The lines are computed from the model.

The computed transient viscosity and first normal stress coefficient during the startup of steady shear are compared with the experimental data in Figs. 3a and 3b, respectively, and the steady-state viscosity and normal stress coefficient as functions of shear rate are compared with the experimental data in Figs. 5a and 5b, respectively. The simulation is noisy at low rates and short times. The model captures the features of the

transient data quite well, including the overshoot and undershoot in the transient viscosity, although the computed magnitudes of the viscosity at intermediate shear rates tend to be low. The model also captures the undershoot in the extinction angle ($\chi = \frac{1}{2}\tan^{-1}(2\boldsymbol{\tau}_{xy}/N_1)$ shown in Fig. 4) that is observed in transient birefringence data. The time scale is about right, and is comparable to the value that would be obtained by fitting λ_H using the location of any peak in the transient viscosity or normal stress coefficient data. The model predictions are in reasonably good agreement with the steady-state data. The logarithmic slope of the computed viscosity function in the power-law region is -0.87 (power-law exponent of 0.13), which is close to, although somewhat larger in magnitude than, the experimental value of -0.82 (power-law exponent of 0.18). The logarithmic slope of the computed normal stress coefficient is -1.45, which is the same as the experimental value. The computed value of $<|\boldsymbol{P}_i\boldsymbol{P}_i|>$ is within 2% of the equilibrium value given by Eq. (9) at low rates, and it increases by only 6% over the range of shear rates shown. Hence, the assumption that the deformation rate term in Eq. (B13) can be neglected is self-consistent with the resulting dynamics. (The computed $<|\boldsymbol{P}_i\boldsymbol{P}_i|>$ exhibits a maximum equal to 110% of the equilibrium value at $\tau_d\dot{\gamma}$ of order 600, after which it decreases as shown in Fig.6.)

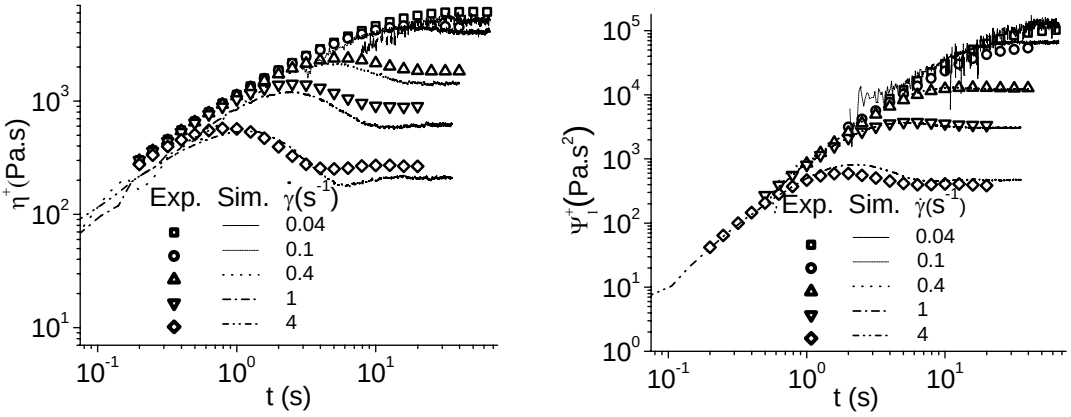

(a) (b)

Fig. 3 Transient growth of (a) viscosity and (b) normal stress coefficient during startup of steady shear.

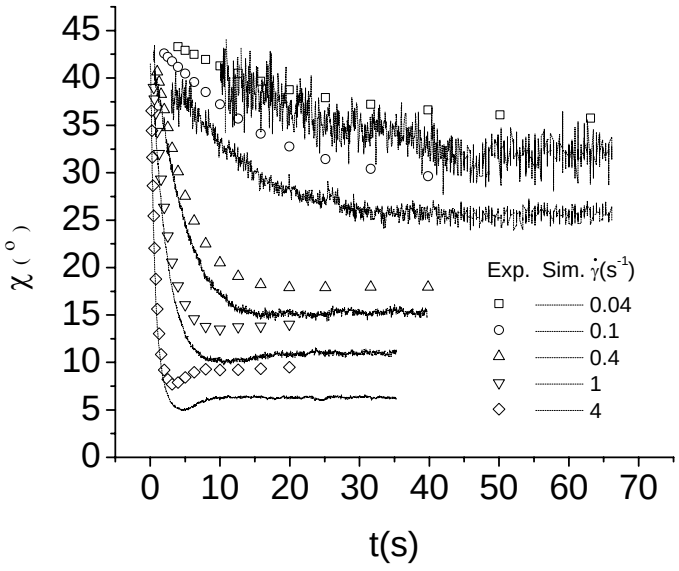

Fig. 4 Transient extinction angle during startup of steady shear

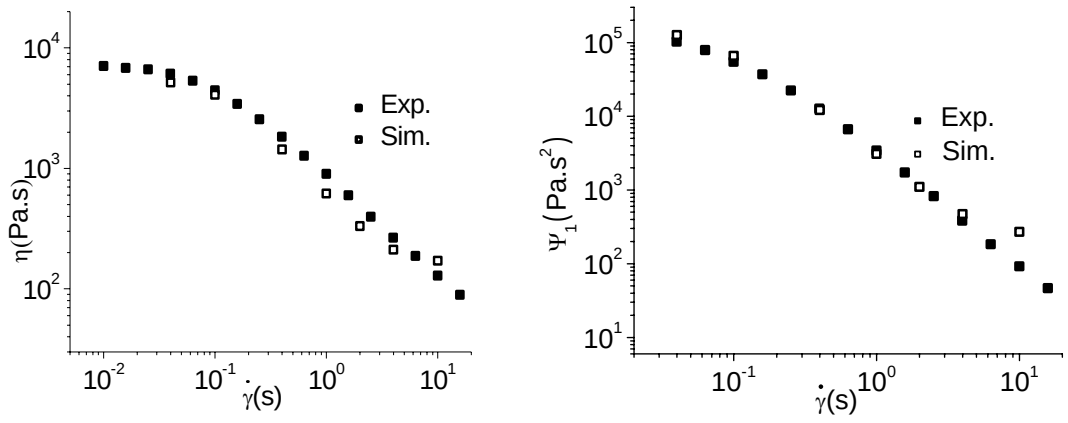

(a) (b)

Fig. 5. Steady-state (a) viscosity and (b) normal stress coefficient as functions of shear rate.

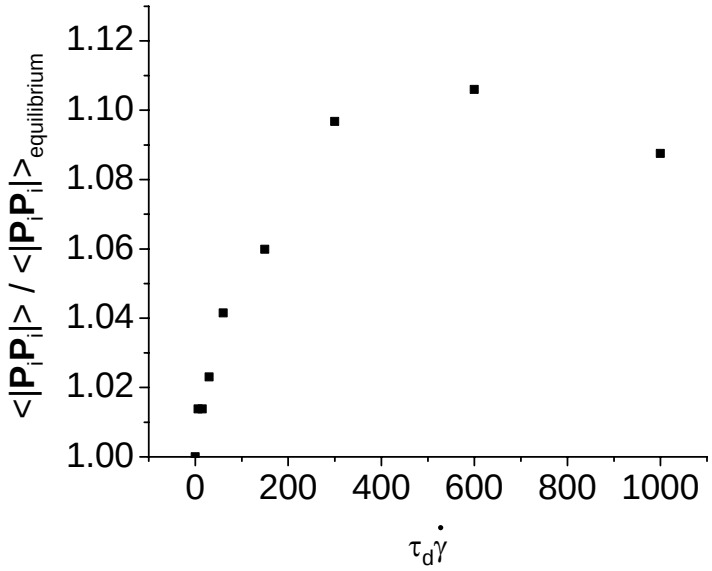

Fig. 6 $<|\boldsymbol{P}_i\boldsymbol{P}_i|>$ normalized with respect to $<|\boldsymbol{P}_i\boldsymbol{P}_i|>$ at equilibrium as a function of dimensionless shear rate.

The average number of segments per chain at steady state computed from the simulation is plotted as a function of dimensionless shear rate in Fig. 7. The number of segments at low rates is roughly one more than the input equilibrium value of nine because of tube segments at the two ends that are smaller than the equilibrium value; these small segments result from chain retraction or the creation of new segments when chain ends leave the tube. The number of segments decreases with increasing shear rate, as expected. The probability distribution of the number of tube segments, shifted so that the distribution is centered about the mean value from Fig. 7 at each value of $\tau_d \dot{\gamma}$, is shown in Fig. 8; the distribution is well approximated by a truncated Gaussian, with a mean of 10.1 and a standard deviation of 2.0, with a slight skewing to a larger number of segments at the highest shear rates. The Guassian distribution is consistent with the random algorithm basically employed in the constraint formation described in section 1.2.8, since according to the central limit theorem, independent random process always tend to a Gaussian distribution. The tube segment length distribution, normalized with respect to the equilibrium length, is shown as a function of segmental position along the tube in Fig. 9. The entanglement spacing is not uniformly distributed, with larger tube segments preferentially located near the center, indicating that entanglements are more likely to be released at the interior of the chain.

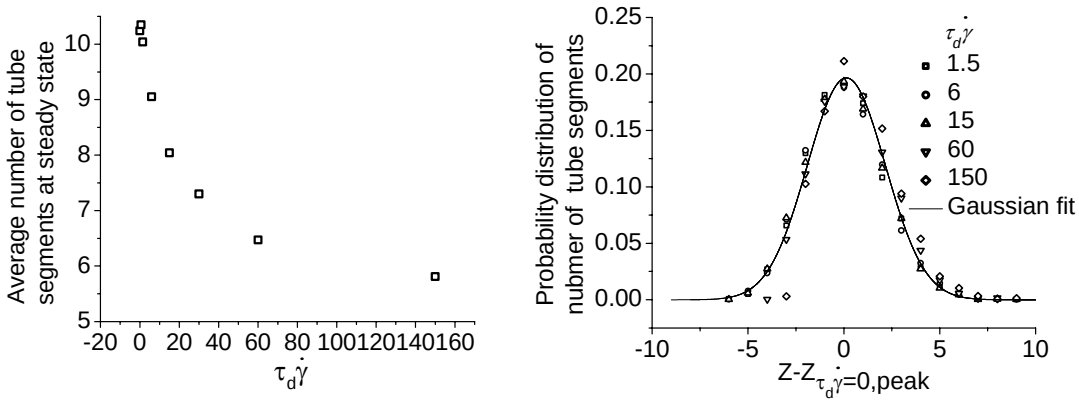

Fig. 7. Average number of tube segments at steady state as a function of dimensionless shear rate.

Fig. 8. Probability distribution of the number of tube segments.

The distribution of loops was estimated by enumerating springs that were directed away from the nearest chain ends and designating these as comprising the "reverse portions" of loops. The probability of finding a spring in the reverse portion of a loop is shown as a function of relative position along the chain in Fig. 10. The loops are uniformly distributed at low rates, but they are concentrated towards the ends of the tube at high rates. This is consistent with a picture in which the chain relaxes from the end to the center.

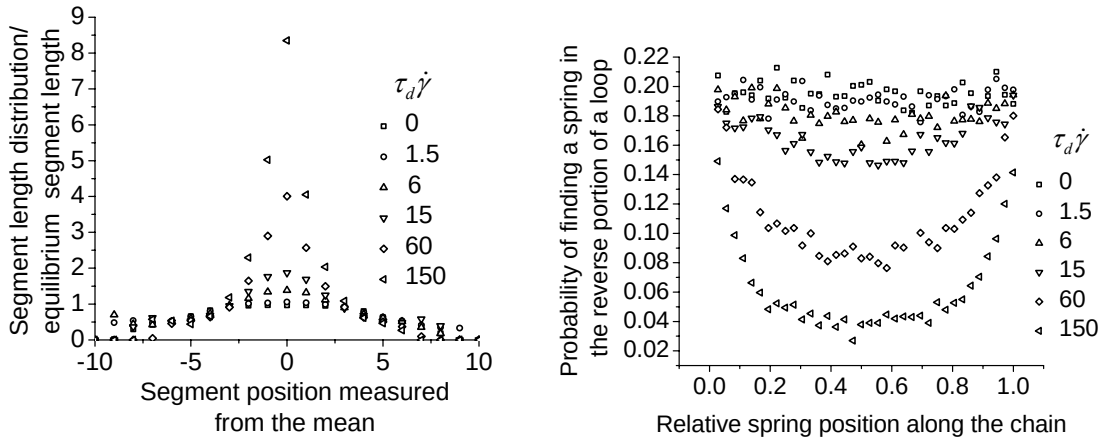

Figure 9. Tube segment length distribution along the chain.

Figure 10. Probability of finding a bead in the reverse portion of a loop as a function of position along the chain.

1.3.2 Sensitivity to the number of beads

The simulation results must be independent of the number of beads for sufficiently large N, since N is simply a coarse-graining parameter without physical meaning. The computed stress in the Hua and Schieber (1999) model (HS model) scales linearly with N at steady state; this is because the model is a one-dimensional projection of the chain on the tube that does not account for the transverse osmotic force. The results for two different values of N computed with the HS model at a specified shear rate are shown in Fig. 11, where the stress is normalized by N. The transients are different, but the two curves in Fig. 11 coincide at the steady-state. The dimensionless value of the shear rate and the maximum length between two adjacent beads both scale with N, corresponding to the characteristic time and characteristic length, respectively.

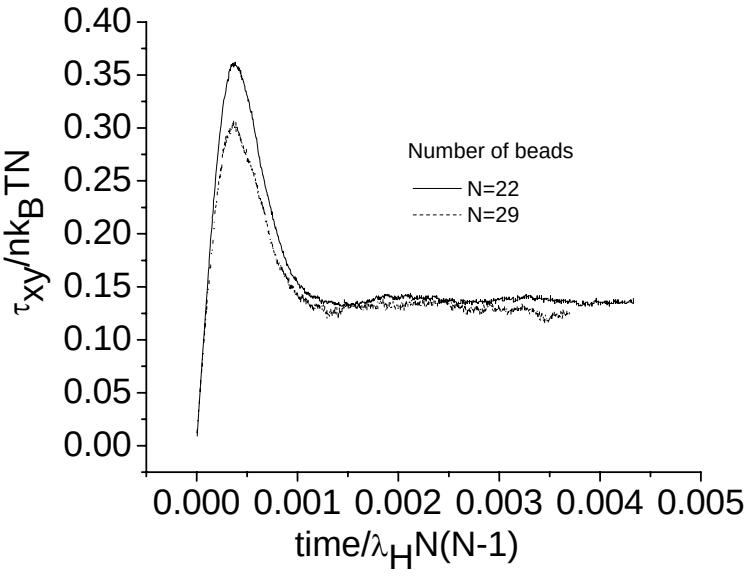

Fig. 11 Comparison of the start-up shear stress of HS model divided by the number of the beads.

Simulation results from the new model at $\tau_d \dot{\gamma} = 15$ are shown in Figs. 12a and 12b for 19, 28, and 37 beads, the last corresponding to N = $4\langle Z\rangle_{eq}$ +1, as used in the simulations shown above. Clearly the result is converged.

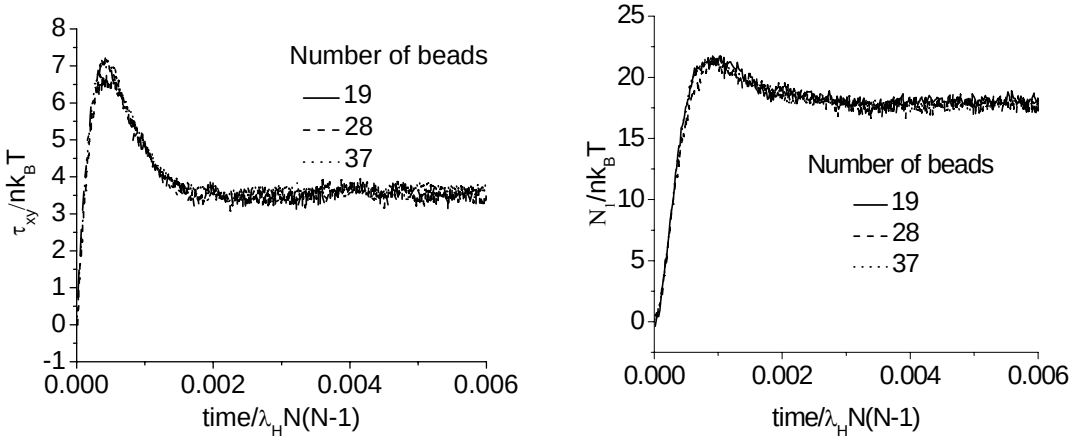

(a) (b)

Fig. 12. Computed transient growth of (a) the viscosity and (b) the normal stress coefficient for 18, 27, and 36 beads.

1.3.3 Experiments of Oberhauser and coworkers

Oberhauser and coworkers (2004) reported rheological measurements for a 4.86 weight % (approx. 5 volume %) solution of polystyrene with a molecular weight of 8.42×10^6 and a polydispersity index of 1.17 in tricresyl phosphate. This fluid had a zero-shear viscosity $\eta_0 = 6.15\times10^3$ Pa·s and a zero-shear first normal stress coefficient $\psi_{1,0} = 9.58\times10^5$ Pa·s^2. The molecular weight between entanglement points is approximately 1.8×10^4 (Ferry, 1980), hence the equilibrium number of segments $\langle Z\rangle_{eq}$ from Eq. 12 is around 13. (Oberhauser and coworkers, using a different method of computation, reported 22 entanglements per chain.) N is again taken equal to be $4\langle Z\rangle_{eq} + 1$.

The magnitude of λ_H was again estimated by simulating the relaxation modulus using Eq. 13 and computing the steady zero-shear properties, giving $\lambda_H = 4.05\times10^{-3}$ s for N = 53, or a Rouse time of 4.52 s. (The Rouse time is 4.22 s and 4.40 s, respectively, if λ_H

is computed from the zero-shear viscosity and zero-shear normal stress coefficient.) The simulated relaxation modulus and the fitted relaxation spectrum are shown in Fig. 13 and table 2, respectively. The fit to the linear viscoelastic data is good in the terminal regime, but deviates in the neighborhood of the crossover frequency; the plateau region fit is not improved by increasing $\langle Z \rangle_{eq}$.

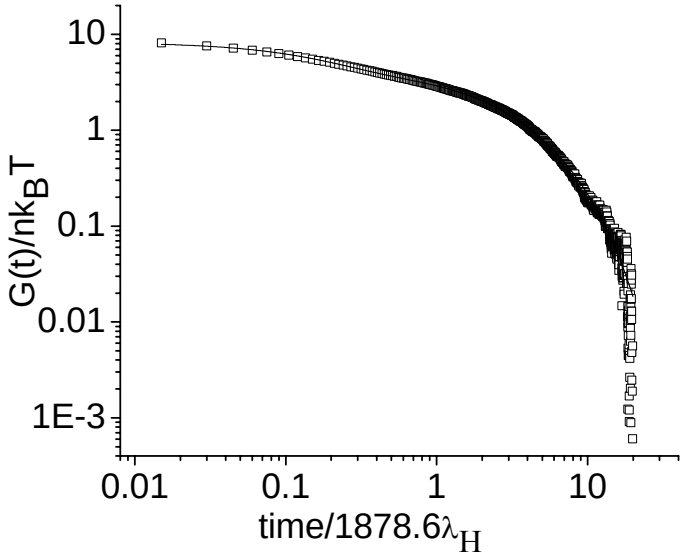

Fig. 13 G(t) computed from the Green-Kubo equation. The line is the three-term fit.

Table 2 Fitted discrete relaxation spectrum for Oberhauser and coworkers' data

Weight factor g_i/nk_BT	Standard error	Time constant $\lambda_i/1878.6\lambda_H$	Standard error
5.578	±0.098	10.504	±0.083
1.768	±0.064	1.049	±0.033
1.219	±0.081	0.141	±0.019

The transient evolutions of the viscosity and normal stress coefficient are shown in Figs. 14a and 14b, respectively, and the steady-state viscosities and normal stress coefficients are shown in Figs. 15a and 15b, respectively. The agreement with the viscosity data at high rates is less satisfactory than for the Venerus and Kahvand data shown above; the computed slope of –0.92 (power-law index of 0.08) in the power-law region is larger in magnitude than the experimental slope of –0.80 (power-law index of 0.20), and the magnitude of the slope would increase even more with increasing $\langle Z \rangle_{eq}$. The computed slope of the first normal stress coefficient in the power-law region is –1.54, compared to an experimental value of –1.50.

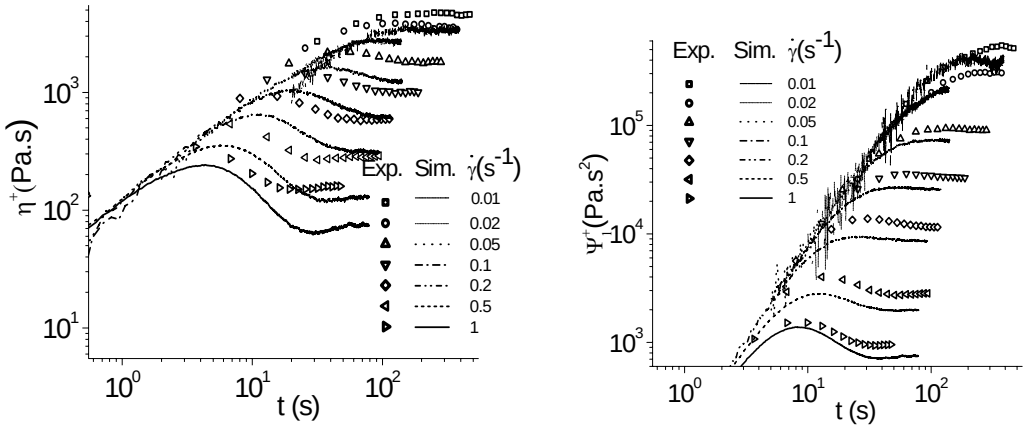

(a) (b)

Figure 14. Transient growth of (a) viscosity and (b) normal stress coefficient during startup of steady shear.

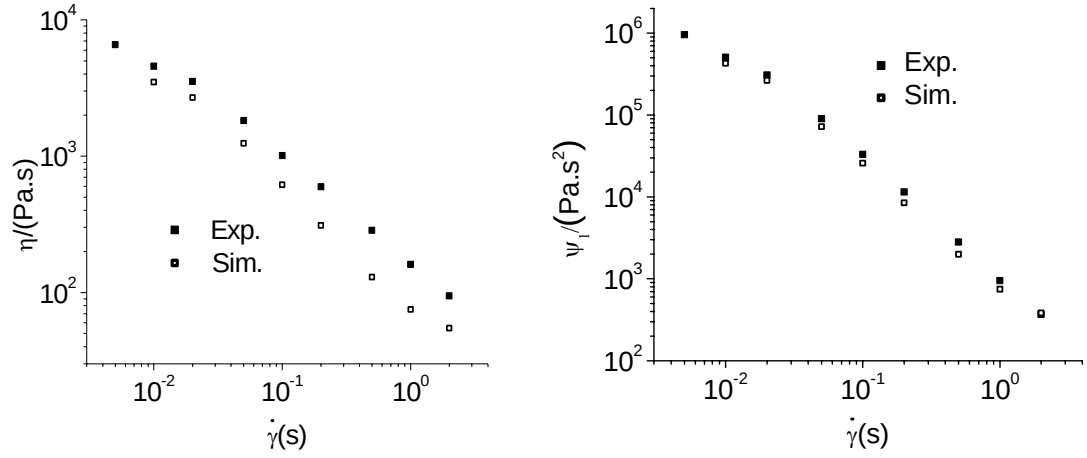

(a) (b)

Figure 15. Steady-state (a) viscosity and (b) normal stress coefficient as functions of shear rate.

1.4 Conclusion

The new full-chain reptation model performs well, especially given that there is only one time-scaling adjustable parameter. The simulation does predict power-law coefficients for the viscosity that are smaller than the experimental values; hence, agreement with the data at high rates deteriorates. The power-law slope is expected to increase with polydispersity, so this trend in the simulations, which assume a monodisperse system, is not surprising, but it points to a potential shortcoming in the use of simulations of this type if even a relatively small amount of polydispersity is unaccounted for. The assumption that the coefficient of the transverse force is always given by the equilibrium value, even at high stresses, could be a contributing factor to the high-rate behavior. Similarly, the assumption that the friction coefficient is independent of position in the tube, which is equivalent to an assumption that the tube diameter is

uniform, could be a contributing factor to the high-rate behavior. This latter assumption is common in tube models, but it ignores the possibility that different parts of the chain may experience different drag because of variations in the local structure of the network. Random forces will dominate the chain motion at low shear rates, so non-uniform drag would have a minimal impact on the viscoelastic properties; conversely, non-uniform drag would become important at high rates.

Finally, the model ceases to be self-consistent as the number of entanglements becomes very small. This is most easily seen by considering a tube that has been reduced by constraint release to a single segment. The chain within the tube would seem to be free of entanglements, yet within the model the chain still experiences the tensile and transverse forces associated with confinement to the tube. There are obvious ways in which this apparent inconsistency can be addressed by special treatment of the portions of the chain contained in the end segments of the tube, but such special treatment appears to be unnecessary for this application as long as the number of entanglements is large. As can be seen from Fig. 7, the fraction of the chain contained in the end segments is small and therefore provides a minor contribution to the stress.

Chapter 2

A stochastic chain simulation of wall slip in entangled polymer melts

2.1. Introduction

Entangled polymer melts and concentrated solutions exhibit apparent wall slip in shear flow at high stresses. This phenomenon was reported as early as 1963 by Benbow and Lamb (1963), who showed photographic evidence of slip and reported a materials-of-construction dependence for the onset of extrusion instabilities. Interest in the subject of wall slip in entangled polymers was renewed following a publication by Ramamurthy (1986) that attributed a delayed onset of extrusion instabilities in brass dies relative to steel dies to different adhesion characteristics at the die wall. The subjects of wall slip and the possible connections between slip and extrusion instabilities are comprehensively reviewed by Denn (2001).

There are two likely explanations for apparent wall slip in entangled polymers. One is adhesive failure at the polymer-die interface. The other is failure at an interior plane because of disentanglement of chains that are bound to the wall from those in the bulk, creating a region near the wall with less resistance to flow. The latter is the more likely explanation of slip prior to the "slip-stick" transition in linear polymers (Wise *et al.*, 2000). The most convincing experiments supporting a disentanglement mechanism are by Durliat and coworkers (1997), who studied the flow of polydimethylsiloxane

(*PDMS*) with a molecular weight of 970,000 over a surface containing grafted PDMS chains of molecular weight 96,000.

Disentanglement seems to have been first proposed as the mechanism for apparent slip by Bergem (1976), and subsequently developed through a scaling argument by Brochard and de Gennes (1992; Brochard *et al.*, 1996). The mental construct is that adsorbed chains at the wall, which are treated as though they are grafted, are entangled with bulk chains that fully penetrate the surface layer. The friction force exerted by the bulk chains, which stretches the surface chains in flow, is balanced by the entropic elastic restoring force of the surface chains. The surface chains cannot be stretched beyond a critical length, after which the balance between friction and elastic forces is achieved by decreasing the number of the entanglements.

Joshi and coworkers (2001; 2002) quantified the disentanglement picture using the tube model developed by Mead, Larson, and Doi (1998), wherein they assumed that the motion of the bulk chains contributes to the relaxation of the tethered chains through convective constraint release, while the motion of the tethered chains has no effect on the bulk chains. They took the grafted layer to have a constant thickness, equal to the equilibrium end-to-end distance of a tethered chain, and they defined the slip velocity as the velocity experienced by tethered chains at the edge of the layer. The model, , which requires the reptation time and the plateau modulus as well as the surface coverage as inputs, predicts a nonmonotonic curve of shear stress versus slip velocity, and agrees qualitatively with the experiments of Durliat and coworkers (1997). Stepanyan and coworkers (2005) carried out an analysis within the same mean-field framework, but using the single-mode Rolie-Poly model (Likhtman and Graham, 2003), and they

obtained similar results. The model of Stepanyan and coworkers also requires the reptation or Rouse time and the surface coverage as inputs, as well as an empirical parameter governing fractional stress transfer between tethered and bulk chains.

We describe here a stochastic chain-level simulation of the flow of an entangled polymeric liquid in the neighborhood of a wall containing grafted chains of the same polymer, although perhaps of a different molecular weight. The simulation is therefore directly relevant to the experiment of Durliat and coworkers, but we believe that it provides insight into the more common situation in which surface chains are adsorbed, not tethered. Our approach is an extension of the stochastic simulation method described in Chapter 1, in which the chain is coarse-grained as a series of beads connected by finitely extensible springs and is confined within a dynamic tube that is composed of segments whose junctions correspond to entanglement points. A single time-scaling adjustable parameter that is proportional to the Rouse time is required to simulate bulk flow. The density of tethered chains is required as an additional model input for the simulation described here. The model is on a more detailed level than the prior analyses, requiring fewer assumptions about the dynamics of the tethered chains.

2.2. Model description

The stochastic model is described in detail in chapter 1. Briefly, each polymer molecule in the ensemble is modeled as a series of N beads connected by N–1 springs. The primitive path is formed by Z segments that have different orientations and lengths, as shown schematically in Fig. 16. Segment junctions represent entanglement points. The configuration of the tube changes with the surrounding flow field, while the length

changes with the length of the confined chain. Because of constraint release and constraint creation, neither the spacing nor the number of segments is constant. The model tracks conjugate constraint pairs and utilizes a self-consistent but mean-field approach to constraint release and renewal. Chain loops within the tube are permitted. Confinement of the chain to the region of the three-dimensional primitive path results in two forces, a tensile force along the chain that prevents chain collapse and a transverse force that keeps the chain within the virtual tube. The dynamics of the chain are governed by these two forces, together with the spring forces, viscous drag forces, and the Brownian forces.

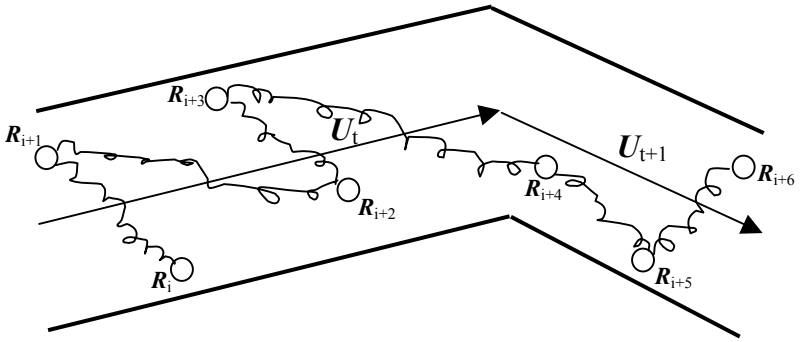

Figure 16. Schematic of the chain in two consecutive tube segments.

In order to apply the model to flow in the vicinity of the wall we consider three types of chains. End-tethered chains at the wall can entangle with themselves and with untethered bulk chains that extend into the wall region; the latter, in turn, can entangle with themselves, with tethered chains, and with chains in the bulk that do not extend into the wall region. The three types of chains are shown schematically in Fig. 17. We

consider two flow regions and allow for the possibility of two distinct shear rates, one near the wall and one in the bulk. There is a choice that has to be made with regard to the free chains that interact with both tethered and bulk chains, since these chains presumably exist partly in one layer and partly in the other. We view their role in the surface layer as being the more important and assign them the same shear rate as the tethered chains. [This is in contrast to the assumption made by Joshi and coworkers (2001; 2002) and Stepanyan and coworkers (2005) that bulk and tethered chains always experience different shear rates.]

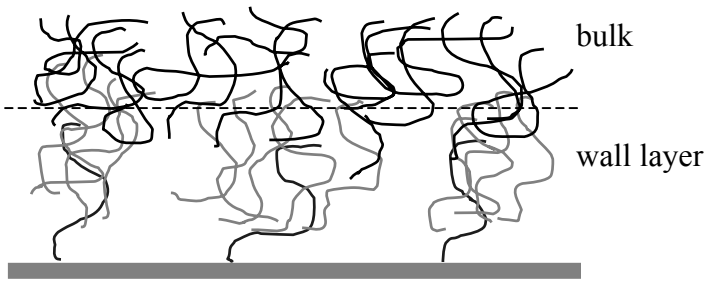

Fig. 17. Schematic of the three types of chains

Two modifications to the stochastic model described by Xu *et al*. (2006) are required for this calculation. First, tethered chains are not permitted to pass through the wall, so beads that would pass through the wall are reflected, using the reflection algorithm described by Hua and Schieber (1998). Second, the chain segment between the point of tethering and the first entanglement is assumed to be free of the tube, hence this segment does not experience either the tensile force or the transverse force.

The shear stress in the wall region is calculated from the projection of the force /unit area $\Sigma \times F_s$ exerted on the wall by the grafted chain, where Σ is the surface coverage

and $\boldsymbol{F}_s$ is the average spring force stored in the first spring. The shear stress is first established for a specified bulk shear rate, and the wall region simulation is then carried out iteratively by adjusting the wall shear rate to obtain the same shear stress as in the bulk (Appendices I and J) . The densities $\boldsymbol{\rho}_b$ of the untethered chains in the wall region and in the bulk are assumed to be the same. For computational purposes, the thickness of the bulk is assumed to be twice the equilibrium brush thickness, which is estimated to be the RMS end-to-end distance $L = \sqrt{N_{kt} b_k^2}$ of a Gaussian chain, where b_k is the length of a Kuhn segment and N_{kt} is the number of Kuhn segments in the tethered chain. The relative numbers of tethered wall chains, untethered chains in the wall region, and untethered chains in the bulk used in the computation are therefore $\frac{\Sigma}{\boldsymbol{L}} : \boldsymbol{\rho}_b : 2\boldsymbol{\rho}_b$.

The thickness of the wall region, which is a function of shear rate, is taken to be the mean location of the last entanglement on the tethered chains, as shown in Fig. 18. (Other choices are possible, since this is not a well-defined physical quantity, and estimates of the slip velocity and slip length using other definitions might vary by up to a factor of five (Appendix K).) The apparent slip velocity is taken to be the extrapolation of the bulk velocity to the wall, using the velocity at the edge of the wall region as the initial value. The extrapolated value is the definition usually used in experiments. The slip length is defined as the distance into the wall by which the bulk velocity profile must be extrapolated in order to reach a velocity of zero; this is the definition conventionally used in experiments.

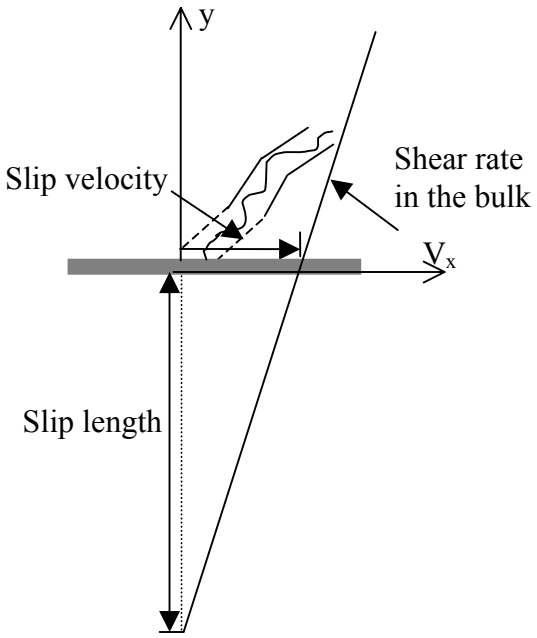

Fig. 18. Definition of the slip velocity and slip length

2.3. Results

2.3.1 Comparison with PDMS data

The data of Durliat and coworkers (1997) on the flow of a PDMS with molecular weight of 970,000 over tethered chains with a molecular weight of 96,000 permit quantitative comparison with the model. Durliat and coworkers treated the surface with a monolayer of chloro-octamethyl-tetrasiloxane to suppress any adsorption of PDMS, so they could be certain that the only surface chains were those that had been grafted to the monolayer. The density of grafted chains was characterized by x-ray reflectometry, and the slip velocity was measured using an optical technique based on near field laser velocimetry, with a penetration depth of the order of 75nm. The slip velocities measured

in this way should not differ by more than five percent from the extrapolated values in the experimental shear-rate range.

The molecular weight between entanglements and the mass density for PDMS are 12,300 and 970 kg/m^3, respectively (Fetters, Lohse *et al.*, 1994). The Kuhn length is 1.2nm. The equilibrium entanglement number for the bulk polymer is Z_{eq} = 79, and the equilibrium entanglement number for the tethered chains is 8. (The code uses only odd numbers for the initial number of entanglements, so the initial number for the tethered chains was set to 7.) The equilibrium thickness of the brush is L = 21 nm (Fetters, Lohse *et al.*, 1994), and the reported surface coverage in the experiments was Σ= 0.022 polymers/nm^2, resulting in 0.6 untethered chains in the wall region and 1.2 untethered chains in the bulk for each tethered chain in the simulation.

Durliat and coworkers (1997) did not include a rheological characterization of the PDMS used in their experiments, so we estimated the time-scaling parameter $\lambda_H = \frac{\varsigma N_k b_k^2}{12 k_B T (N-1)}$ using a value η_0 = 59,000 Pa.s for the zero-shear viscosity of the bulk polymer; this value was obtained by extrapolation of data from the same research group in Fig. 5 of Leger *et al*. (1996). (Here, ζ is the bead friction coefficient, which is the only adjustable parameter; b_k is the Kuhn length; and N_k is the number of Kuhn lengths in the chain.) The value we obtain in this way for N = 159 (N = $2Z_{eq}$ + 1) is $\lambda_H = 5.8\times10^{-7}$ s, corresponding to a Rouse time of $1.5\text{x}10^{-3}$ s for the entire chain. The calculated steady-state flow curve for the bulk PDMS is shown in Fig. 19. The melt is highly shear thinning, and there is a transition to a stress plateau at a shear rate of about 2 s^{-1}. The stress plateau is typical of highly entangled linear polymer melts (Bercea et al.,

1993; Pattamaprom and Larson, 2001; Inn *et al*., 2005). [An alternative calculation of λ_H utilized a modulus G_N^0 = 200,000 Pa (Fetters *et al.,* 1994), from which we calculated the disengagement time $\tau_d = \frac{12}{\pi^2}\frac{\eta_0}{G_N^0} = 0.36s$. We then fit the time constant λ_H by computing the relaxation modulus using a Green-Kubo linear response equation, as in Xu *et al*. (2006), and using the resulting spectrum to compute τ_d. The corresponding value of λ_H was 3.2x10^{-7} s, giving in a zero-shear viscosity that was about 40% lower than the value obtained from the extrapolated data.]

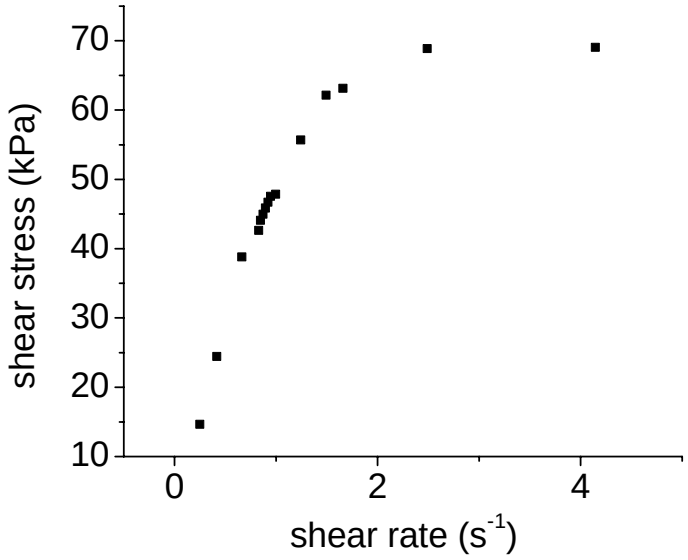

Fig. 19. Computed steady-state flow curve for 970,000 molecular weight PDMS.

We assume that the friction coefficient for beads on tethered and untethered chains is the same, and we keep the same ratio of N_k/(N - 1) for tethered and untethered chains; hence, the value of λ_H is the same for all chains in the simulation. There are two sources of computational uncertainty in the simulation. One is the effect of ensemble

size. The other is the effect of imperfect stress matching between the bulk and the wall region. The latter is the more significant, and it was estimated by fitting the computed wall shear rate as a function of bulk shear stress and using the slope of the fitted curve to estimate the uncertainty in the wall shear rate and wall region thickness. The maximum deviation between the wall and bulk stresses in all calculations was 4.9%, and the average was 1.7%.

The computed slip velocity is shown in Fig. 20 as a function of the shear rate in the bulk, together with the experimental data of Durliat *et al*. (1997). The experimental uncertainty is not shown, but it is comparable in size to that in the simulations. The simulation shows a sharp rise in the slip velocity at a shear rate near 1, increasing from values of less than 1 μm s^{-1} to a saturated value of about 250 μm s^{-1}. The data show a similar transition, with the same apparent saturation value, but the shear-rate dependence of the slip velocity prior to the transition is weaker, and the transition occurs at a shear rate of about 5 s^{-1}. In addition, the data suggest a small multi-valued region in the slip velocity curve that is not seen in the simulation (The simulation is shifted to the right on the shear-rate axis by about a factor of two if λ_H is set equal to 3.2×10^{-7} s, as discussed a above.)

The computed slip length is shown as a function of the computed slip velocity in Fig. 21, together with the experimental data. The slip length increases in a nearly linear fashion, from a value of order 2 μm at low slip velocities to a value of 30 μm (experiment) to 100 μm (simulation) following the transition. The simulation and the data are roughly parallel in the region of increase, but the simulation shows linear behavior over the entire range, whereas the data show a constant slip length at low slip velocities.

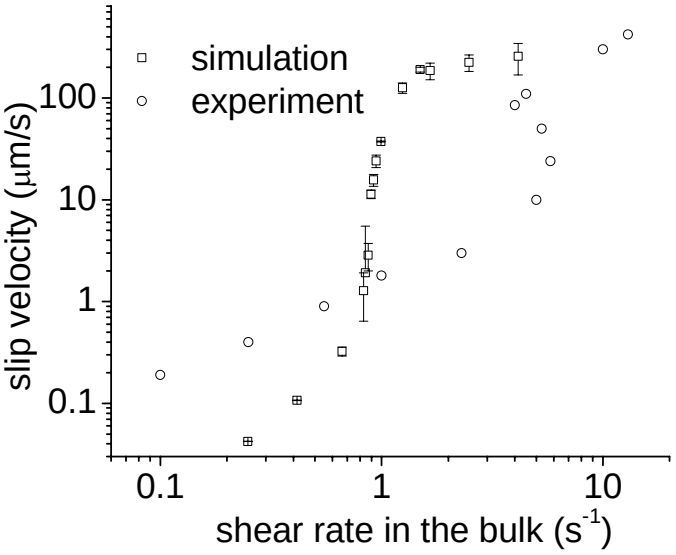

Fig. 20. Slip velocity as a function of shear rate in the bulk

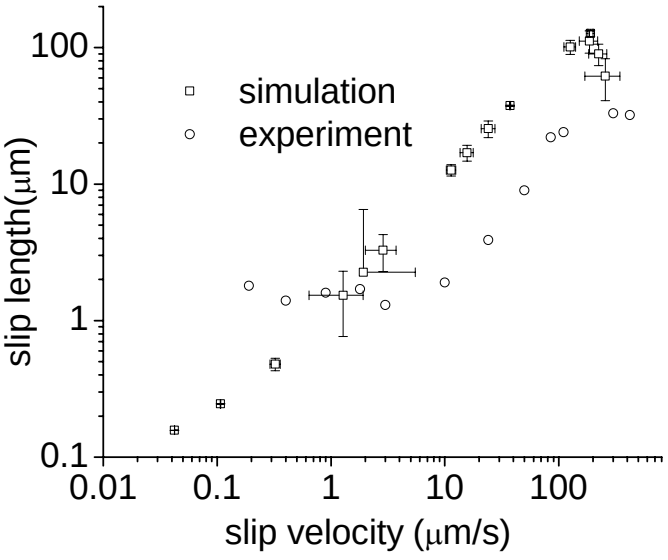

Fig. 21. Slip length as a function of slip velocity

The computed mean orthogonal distance from the wall to the end of the tethered chains is shown as a function of shear rate in Fig. 22. The thickness of the wall layer defined in this manner decreases from about 13 nm (roughly 2L/3) at the lowest shear rates employed in the simulation to a plateau value of about 3 nm. (This definition of the thickness of the wall layer is reasonable, but it is not the only definition that might be chosen within the framework of the simulation. Other definitions, such as the mean orthogonal distance to the first entanglement of the tethered chains, will give results that differ quantitatively but not qualitatively. The latter definition would increase the deviation between simulation and experiment, however.)

The computed mean number of entanglements on the tethered chains is shown as a function of shear rate in Fig. 23. The number of entanglements for the tethered chains at low shear rates is greater than the nominal equilibrium value of seven (or eight). An increase of about one entanglement/chain is expected because of small segments at the chain end that result from chain retraction or the creation of new segments when chain ends leave the tube (Chapter 1). The larger increase seems to suggest that the presence of the much longer bulk chains in the wall region increases the probability that entanglements including wall chains will be formed as compared to an ensemble consisting only of the shorter chains. (The reflection algorithm that comes into play when a segment of the tethered chain intersects the wall causes a discontinuous slope in the tube profile, which is treated as a new entanglement in the algorithm, hence overcounting the number of entanglments; this is an artifact that we did not consider to be sufficiently important to warrant modifying the algorithm.)

The entanglement number for tethered chains decreases substantially with increasing shear rate, reflecting the greater chain extension in the wall region; this is the cause of the large increase in the slip velocity, as hypothesized by Bergem (1976). Comparison of Figs. 22 and 23 shows that the projected chain length is approximately proportional to the number of entanglements, while comparison with Fig. 19 shows that the average number of entanglements about the tethered chains decreases nearly linearly with the bulk shear stress.

The entanglement density is defined as the number of entanglements divided by tube length (i.e., $Z/\sum_{t=1}^{Z}|\boldsymbol{U}_t|$). The ratio of the entanglement density around tethered chains to that around bulk chains is shown in Fig. 24. The ratio is slightly greater than unity at low rates, where tube deformation is small. (The ratio is greater than unity because of the greater relative propensity for entanglements in tethered chains resulting from the presence of the large bulk chains, because the tethered chains will always be stretched more than bulk chains at corresponding bulk shear rates, and because of the reflection algorithm.) The wall chains become progressively less entangled with increasing shear rate, however, and the entanglement density ratio reaches a plateau value of around 0.4, reflecting the greater loss of entanglements in the wall region.

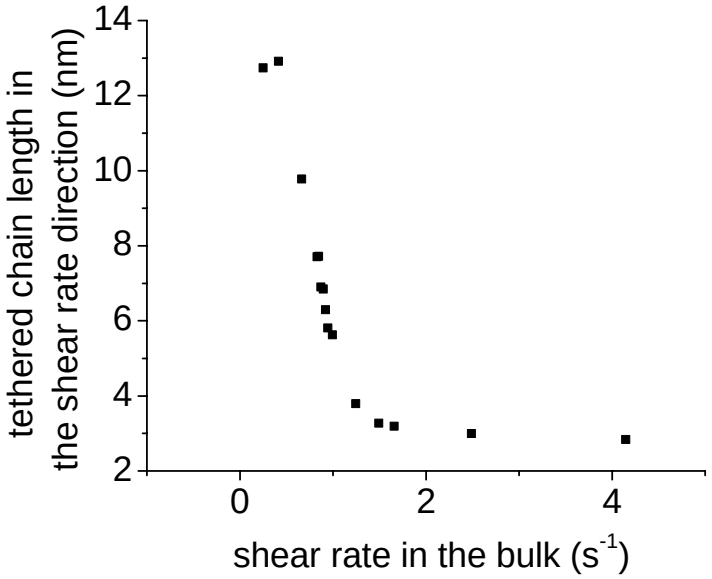

Fig. 22. Tethered chain projected length normal to the wall as a function of bulk shear rate.

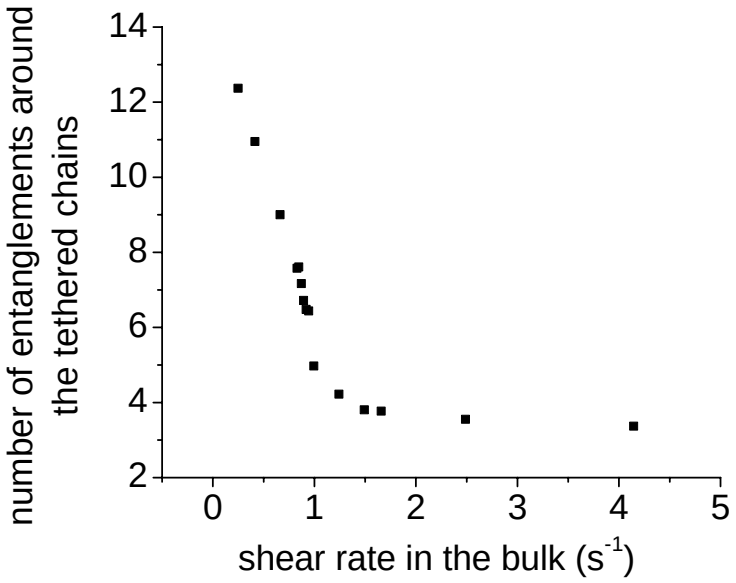

Fig. 23. Mean number of entanglements per tethered chain as a function of bulk shear rate.

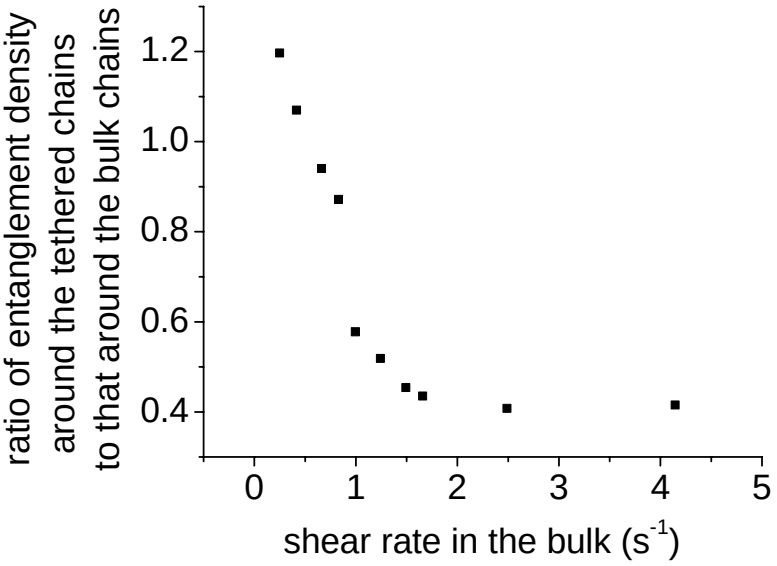

Fig. 24. Ratio of entanglement density for tethered chains to entanglement density for free bulk chains.

2.3.2 Comparison with polybutadiene data

Mhetar and Archer (1998a) carried out slip measurements on a series of narrow-distribution 1,4-polybutadiene (*PBDE*) melts in plane Couette flow, where they used tracer particle velocimetry with a spatial resolution of 0.5 μm to measure the slip velocity. They performed one test with a bulk polymer with a molecular weight of 176,400 and surface grafted chains of equal length (Mhetar and Archer, 1998b), but the grafting density was not measured and the surface was not treated to prevent chain adsorption. The slip velocity for this one case was slightly less with the grafted surface chains than with the surface without grafting, where the wall chains were presumably adsorbed.

We have carried out simulations using the properties of a PBDE with a molecular weight of 67,300 and three surface chain molecular weights: 67,300, 32,600 and 15,200.

The first wall molecular weight would correspond to strong adsorption at the chain ends, which is the situation assumed in the simulation; the two smaller molecular weights might be envisioned as reflecting different adsorbed lengths of the surface chains, hence correspondingly shorter tails. The entanglement molecular weight and mass density for polybutadiene at 25°C are 2,100 and 910 kg/cm^3, respectively (Ferry, 1980); hence, the equilibrium entanglement number for the bulk chain and the initial entanglement numbers for the grafted chains are 31, 31, 15, and 7, respectively. The effective grafted density is unknown, and we used a value of 6×10^{-3} monomers per unit surface area; the monomer size of polybutadiene is around 0.5 nm, so the input surface chain density Σ was 0.024 polymers/nm^2. The equilibrium thicknesses of the brushes for three surface molecular weights are 25nm, 17nm and 12nm, respectively, in which case the corresponding ratios of tethered chains to untethered chains in the wall region to untethered chains outside the wall region for the computations are 1:8:16, 1.4:8:16, and 1:4:8, respectively.

Mhetar and Archer (1998a) report a zero-shear viscosity of $7.53\text{x}10^3$ Pa-s, an equilibrium modulus of $7.87\text{x}10^5$ Pa, and a reptation time of 0.022s for this bulk polymer. If we take the equilibrium modulus to be G_N^0 and use the equation $\tau_d = \frac{12}{\pi^2}\frac{\eta_0}{G_N^0}$ we obtain a value of τ_d = 0.012s. Bulk simulations in which λ_H was computed using either this value of τ_d or the reptation time reported by Mhetar and Archer resulted in an underestimation of the computed zero-shear viscosity. We therefore chose to match η_0 in the simulation in order to compute λ_H, resulting in a computed value of $\lambda_H = 4.8\times10^{-7}$ for N = 63 (corresponding to a Rouse time of $7.6\text{x}10^{-4}$ s). The computed steady-state shear

stress is shown as a function of shear rate in Fig. 25. The first two computed points are in the low-shear Newtonian region. There is no plateau in the shear stress in the shear-rate range studied, which is the range relevant to the experiments.

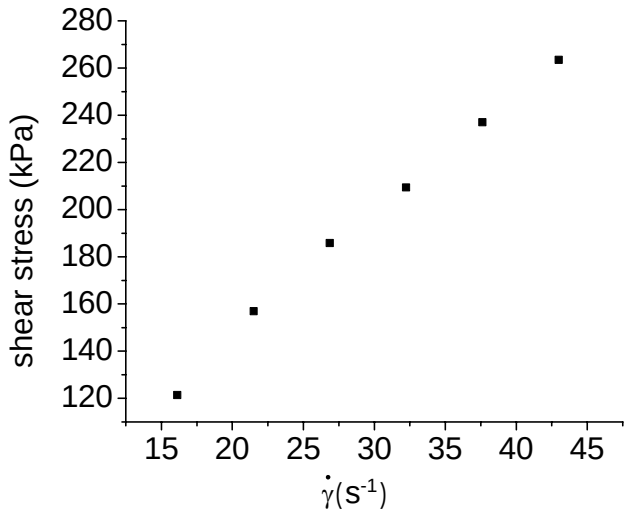

Fig. 25. Computed steady-state flow curve for 67,300 molecular weight PBDE.

The computed slip velocity is shown in Fig. 26 as a function of shear stress for the three different surface-chain molecular weights, together with some of the data of Mheta and Archer(1998a). The computed slip velocities range from 10-130 μm/s over the stress interval 120-260 kPa for the 67,300 M_w tethered chains, with higher values for the shorter wall chains. The experiments, which were carried out at lower stresses, exhibit about the same slope as the calculations, and the experimental values of 40-50 μm/s at the highest stresses are consistent with the calculations for the 67,300 tethered chains. There is no obvious transition in the computed slip velocity of the type seen in Fig. 20 for the PDMS. Mehtar and Archer (1998a) saw no transition at this molecular weight.

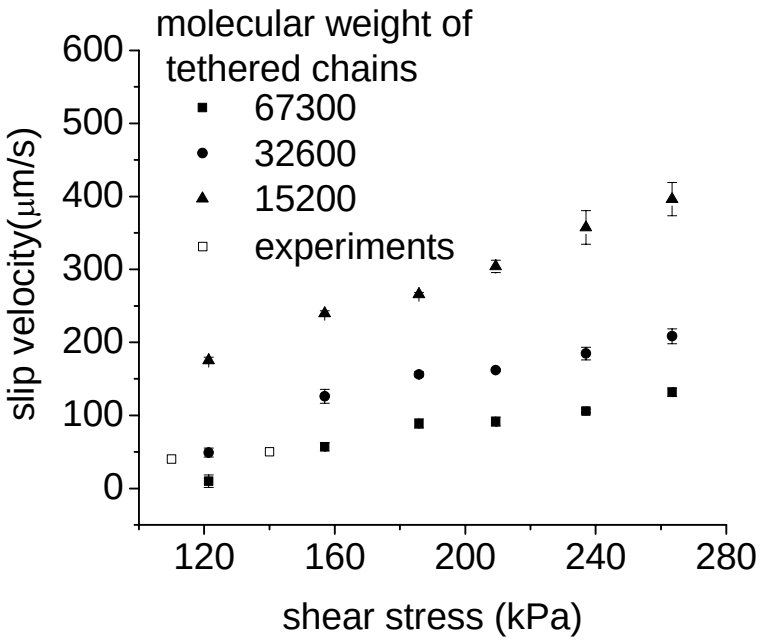

Fig. 26. Calculated slip velocity as a function of shear stress for different surface chain molecular weights, together with data of Mhetar and Archer (1998a).

The computed slip lengths are shown in Fig. 27. There is a maximum in the computed slip length for all three wall chain lengths, followed by roughly constant values for stresses above 2×10^5 Pa. Mehtar and Archer (1998a) reported a slip length of 2.4 μm for this polymer, which was not tethered; this is comparable to the computed value for the longest surface chain. The average high-stress value of the computed slip length is plotted versus the molecular weight of the grafted polymer in Fig. 28, where we find a power law with a scaling exponent of – 0.82.

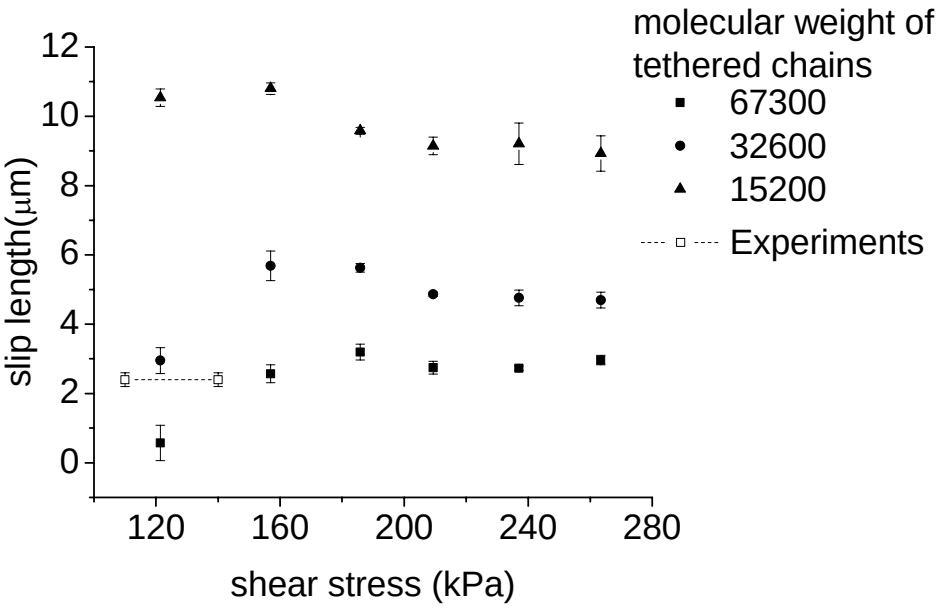

Fig. 27. Calculated slip length as a function of shear stress for three different surface chain molecular weights, together with data of Mhetar and Archer (1998a).

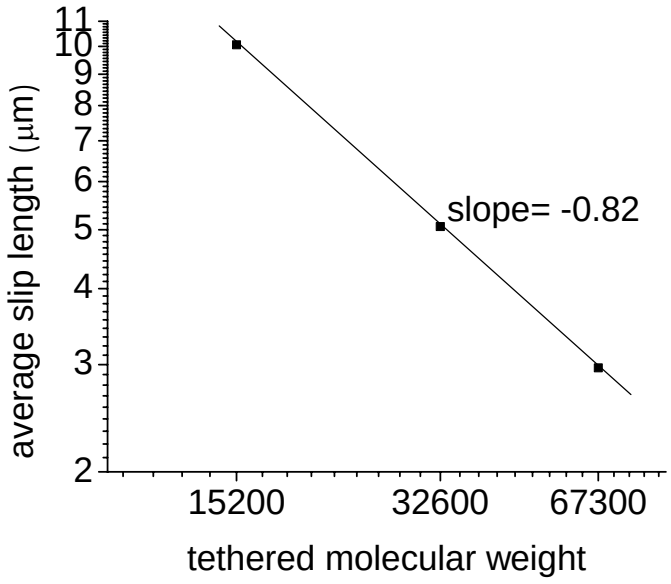

Fig. 28. Average high-stress slip length as a function of tethered chain molecular weight.

2.4. Discussion

The PDMS data are a direct test of the applicability of the model to understanding apparent wall slip, and the results are positive. The computed slip velocities and slip lengths are of the same magnitude as the experimental values, and the functional forms are close to those seen in the experiments. There are differences between the way slip velocities are measured in the experiments, which are limited by the 75 nm penetration length, and the way in which they are computed in the simulation, in which there is an inherent degree of ambiguity in the selection of the precise location for the edge of the wall region. These differences, as well as the uncertainty in the estimate of the time-scaling parameter (or, equivalently, the estimate of the chain Rouse time), could account for some of the differences between the data and the calculations. It is more likely, however, that inherent limitations in the model are the primary factor. First, the model utilizes an overly simple picture of the wall region by using only two compartments and three types of chains. Second, there are obvious physical assumptions that cannot be rigorously correct that have been made to retain model simplicity; perhaps the most important are the assumption that the relative densities of tethered chains and wall-region bulk chains are unaffected by chain extension and wall layer compression as the shear rate is increased, and the absence of a mechanism by which the surface brush expels the bulk chains when the surface coverage exceeds a critical value. Despite these limitations, the model appears to capture the essential physical phenomena in a meaningful way.

The PBDE simulations address data that are more reflective of the real polymer processing situation, wherein the wall chains are adsorbed, not tethered, and they have an unknown distribution of lengths with an average that is shorter than that of the bulk

chains. The simulations could have been tuned, through selection of the unknown surface density and the tethering length, to bring the observations and the experiments into closer agreement. A higher surface chain density is clearly needed, for example, since the closest agreement between the simulations and the data is for a tethered chain that is equal in length to the bulk chains. Such tuning does not seem to be warranted in the current situation, however, where we seek understanding, not forced agreement with a limited set of data. In that respect, the fact that the computations are of the same magnitude and functionality as the experimental data from an experiment in which the key parameter is uncontrolled is quite positive.

Overall, we believe that the agreement between both sets of experiments and the model calculations are quite good, especially considering the simplicity of the model structure and the minimal input data required (the surface coverage and one characteristic time for the bulk polymer). The power-law dependence of the slip length on the wall chain length suggests that the equivalent tethered chain length could be estimated by using an adsorption theory to calculate the distribution of adsorbed lengths, and then using the power-law dependence as a weighting factor in averaging over the distribution.

2.5. Conclusions

The stochastic chain model provides fundamental insight into the mechanism of apparent wall slip in entangled polymer melts. Apparent slip is a consequence of a rapid decrease in the entanglement density for chains in the region of the wall. The good agreement between model predictions and PDMS experiments in which a wall layer with a known density of tethered chains contacts a bulk melt supports the notion that the

model captures the essential physics of the wall processes, although important details related to a change in the effective density of bulk chains in the wall region are neglected. The model cannot provide quantitative information about apparent slip when chains are simply adsorbed at the wall, since the surface density and effective chain length are required inputs to the calculation; the model does agree in broad terms with experiments on PBDE, however.

APPENDIX A. Derivation of Tensile force

It is well known that the conformational distribution function for any flexible chain with square of end-end distance L^2 is

$$\Psi_{end-end}(L) \propto \exp(-\frac{3L^2}{2N_k a_k^{\ 2}}). \qquad \text{(A1)}$$

regardless of the density of the other chains surrounding it, as long as the chain is only subject to thermal motion. One intuitively visualizes that the chain must experience different forces when it moves in a dilute or a highly concentrated solution, however. In order to verify if there are extra forces acting on the chain in an entangled state, we first need to answer a different question, that is, what is the conformational distribution function for a chain having a length L in a particular direction, such as along a confined tube? This is a distinct concept for a chain moving in a network compared to one moving in a free space. We also want to emphasize that this chain length L is not the same as the square root of the end-end chain distance L that was used in equ(A1) since the chosen direction is not always the direction connecting two ends of the chain. Doi (1998) gives that statistical distribution function as

$$\Psi(L) \propto \exp[-\frac{3}{2N_k a_k^{\ 2}}(L-\overline{L})^2], \qquad \text{(A2)}$$

where $\overline{L}$ is defined as the contour length of the tube,

$$\overline{L} = \sqrt{ZN_k a_k^2} \qquad \text{(A3)}$$

On the other hand, the distribution function of the same polymer chain in free space is

$$\Psi^{free}(L) \propto \exp(-\frac{3L^2}{2N_k a_k^{\ 2}}). \qquad \text{(A4)}$$

which is identical to equ(A1), although L in the two equations has different meanings. Hence, the length term $\overline{L}$ in Eq. (A2) accounts for the constraint induced by the polymer network.

The force F along the chain can be calculated by the usual procedure for the derivation of the force law for a Hookean spring (Bird, Armstrong *et al.*, 1987). Specifically, we start with the Helmholtz free energy of the chain with fixed end points,

$$A = -k_B T \ln \Psi(L). \qquad \text{(A5)}$$

If one end is allowed to move isothermally, while the other end remains fixed, the work FdL for the free end to be extended for an amount dL must equal the decrease in the Helmholtz free energy of the system:

$$FdL = -dA = k_B T d \ln \Psi(L) = 3k_B T(\frac{L-\overline{L}}{N_k a_k^2})dL. \qquad \text{(A6)}$$

Hence,

$$F = \frac{3k_B T}{N_k a_k^2} L - \frac{3k_B T}{N_k a_k^2} \bar{L} \qquad \text{(A7)}$$

The first term on the right hand of Eq. (A6) is the force law for a Hookean spring in free space; the second term is the tension force F^T that is induced by the confined environment. This force prevents the chain from collapsing in the tube. Equation (4) then follows immediately.

APPENDIX B. Derivation of the repulsive force.

The Langevin Equations (1) have the following form after inserting the expressions for $F^{\mathrm{s}}, F^{\mathrm{B}}, F^{\mathrm{T}}$, and F^{R} from Eqs. (2), (3), (4), and (7), respectively:

$$0 = -\zeta(d\boldsymbol{R}_i - \boldsymbol{\kappa}\cdot\boldsymbol{R}_i dt) - \sum_{j=1}^{N} A_{ij} H\boldsymbol{R}_j dt - \alpha_i \boldsymbol{P}_i dt - \left|\boldsymbol{F}^T\right|\delta_{i1}\boldsymbol{u}_{t(1)} + \left|\boldsymbol{F}^T\right|\delta_{iN}\boldsymbol{u}_{t(N)} + \sqrt{2k_B T\zeta}\, d\boldsymbol{W}_i \tag{B1}$$

where the Rouse matrix $A_{ij} = \begin{cases} 2 & i = j \\ -1 & i = j \pm 1 \\ 0 & otherwise \end{cases}$, and subscripts $t(1)$ and $t(\mathrm{N})$ denote the indexes of the tube segments in which the 1st and N^{th} beads are located. We are interested only in the chain behavior for a small displacement from equilibrium, so the FENE springs can be replaced by Hookean springs. The differentials of Eqs. (5) and (6) give the following expressions for ds_i and $d\boldsymbol{P}_i$, respectively:

$$ds_i = \boldsymbol{u}_t \cdot d\boldsymbol{R}_i + \boldsymbol{R}_i \cdot d\boldsymbol{u}_t \tag{B2}$$

$$d\boldsymbol{P}_i = d\boldsymbol{R}_i - \boldsymbol{u}_t ds_i - s_i d\boldsymbol{u}_t \tag{B3}$$

where we write $\boldsymbol{u}_t$ in place of the more cumbersome $\mathbf{u}_{t(i)}$ whenever here is no ambiguity, and

$$d\boldsymbol{u}_t = (\boldsymbol{\delta} - \boldsymbol{u}_t\boldsymbol{u}_t)\cdot\boldsymbol{\kappa}\cdot\boldsymbol{u}_t dt \tag{B4}$$

Combining Eqs. (5), (6), (B1), (B2), (B3), and (B4) then gives

$$ds_i = s_i \boldsymbol{\kappa} : \boldsymbol{u}_t \boldsymbol{u}_t dt + \boldsymbol{u}_t \cdot (\boldsymbol{\kappa} + \boldsymbol{\kappa}^T) \cdot \boldsymbol{P}_i dt - \frac{1}{4\lambda_H} \sum_{j=1}^{N} A_{ij} s_j dt - \frac{\left|\boldsymbol{F}^T\right|}{\zeta} \delta_{i1} \boldsymbol{u}_{t(1)} dt + \frac{\left|\boldsymbol{F}^T\right|}{\zeta} \delta_{iN} \boldsymbol{u}_{t(N)} dt + \sqrt{\frac{2k_B T}{\zeta}} \boldsymbol{u}_t \cdot d\boldsymbol{W}_i \quad \text{(B5)}$$

and

$$d\boldsymbol{P}_i = \boldsymbol{\kappa} \cdot \boldsymbol{P}_i dt - \frac{1}{4\lambda_H} \sum_{j=1}^{N} \overline{A}_{ij} \boldsymbol{P}_j dt - \boldsymbol{u}_t \boldsymbol{u}_t \cdot (\boldsymbol{\kappa} + \boldsymbol{\kappa}^T) \cdot \boldsymbol{P}_i dt + \sqrt{\frac{2k_B T}{\zeta}} (\boldsymbol{\delta} - \boldsymbol{u}_t \boldsymbol{u}_t) \cdot d\boldsymbol{W}_i \quad \text{(B6)}$$

Here,

$$\lambda_{\boldsymbol{H}} \equiv \frac{1}{4} \frac{\zeta N_{\boldsymbol{K}} a_{\boldsymbol{K}}^{\,2}}{3k_{\boldsymbol{B}} T(N-1)} = \frac{\zeta}{4H} \quad \text{(B7)}$$

$$\overline{A_{ij}} = A_{ij} + \lambda_{\boldsymbol{H}} \frac{\alpha_i}{\zeta} \delta_{ij} \quad \text{(B8)}$$

We now transform to normal modes to solve Eq. (B6). Let Ω be the orthogonal matrix that diagonalizes $\overline{A}$ and let $\{b_i\}$ be the eigenvalues of $\overline{A}$; i.e.,

$$\sum_{k=1}^{N} \Omega_{ik} \Omega_{jk} = \delta_{ij} \quad \text{(B9)}$$

and

$$\sum_{k,m=1}^{N} \Omega_{ik} \overline{A}_{km} \Omega_{mj} = b_i \delta_{ij} \quad \text{(B10)}$$

Define

$$\boldsymbol{P}_i = \sum_{i=1}^{N} \Omega_{ik} \hat{\boldsymbol{P}}_k \,, \quad \text{(B11)}$$

in which case

$$\hat{\boldsymbol{P}}_k = \sum_{i=1}^{N} \Omega_{ki} \boldsymbol{P}_i \,. \quad \text{(B12)}$$

Then Eq. (B6) can be written

$$d\hat{\boldsymbol{P}}_k = \boldsymbol{\kappa}\cdot\hat{\boldsymbol{P}}_k dt - \frac{1}{4\lambda_H} b_k \hat{\boldsymbol{P}}_k dt - \sum_{i=1}^{N} \Omega_{ki}\boldsymbol{u}_{t(i)}\boldsymbol{u}_{t(i)}\cdot(\boldsymbol{\kappa}+\boldsymbol{\kappa}^{\mathrm{T}})\cdot\boldsymbol{P}_t dt + \sqrt{\frac{2k_BT}{\zeta}}\sum_{i=1}^{N}\Omega_{ki}(\boldsymbol{\delta}-\boldsymbol{u}_{t(i)}\boldsymbol{u}_{t(i)})\cdot d\boldsymbol{W}_i$$

(B13)

At equilibrium, or for nonequilibrium flows for which $\|\boldsymbol{\kappa}\|\lambda_H$ <<1, the terms in Eq. (B13) involving $\boldsymbol{\kappa}$ can be neglected, and the stochastic differential equation can be solved to obtain the following averages:

$$<\hat{\boldsymbol{P}}_i\hat{\boldsymbol{P}}_j>=\frac{8k_BT\lambda_H}{\varsigma(b_i+b_j)}\delta_{ij}\sum_{q=1}^{N}\Omega_{iq}\Omega_{jq}<\boldsymbol{\delta}-\boldsymbol{u}_{t(q)}\boldsymbol{u}_{t(q)}>=\frac{N_K a_K{}^2}{3(N-1)b_i}\delta_{ij}\sum_{q=1}^{N}\Omega_{iq}\Omega_{jq}<\boldsymbol{\delta}-\boldsymbol{u}_{t(q)}\boldsymbol{u}_{t(q)}>$$

(B14)

At equilibrium, $\boldsymbol{u}_t$ is an independent and random vector for all segments, from which it follows that $<\boldsymbol{\delta}-\boldsymbol{u}_{t(q)}\boldsymbol{u}_{t(q)}>$ must be equal to $2\boldsymbol{\delta}/3$. In that case, Eq. (B14) can be written

$$<\hat{\boldsymbol{P}}_i\hat{\boldsymbol{P}}_j>=\frac{2N_K a_K{}^2}{9(N-1)b_i}\delta_{ij}\sum_{q=1}^{N}\Omega_{iq}\Omega_{jq}\boldsymbol{\delta} \qquad \text{(B15)}$$

$$<\boldsymbol{P}_k\boldsymbol{P}_m>=\sum_{i,j=1}^{N}\Omega_{ik}\Omega_{jm}<\hat{\boldsymbol{P}}_i\hat{\boldsymbol{P}}_j>=\frac{2N_K a_K{}^2}{9(N-1)}\delta_{ij}\sum_{i,j=1}^{N}\frac{\Omega_{ik}\Omega_{jm}}{b_i}\sum_{q=1}^{N}\Omega_{iq}\Omega_{jq}\boldsymbol{\delta}$$
$$=\frac{2N_K a_K{}^2}{9(N-1)}C_{km}\boldsymbol{\delta} \qquad \text{(B16)}$$

where $C = \overline{A}^{-1}$. Then

$$< (\boldsymbol{P}_{i+1} - \boldsymbol{P}_i)(\boldsymbol{P}_{i+1} - \boldsymbol{P}_i) >= \frac{2N_K a_K{}^2}{9(N-1)} \left[C_{i+1,i+1} - C_{i,i+1} - C_{i+1,i} + C_{i,i} \right] \boldsymbol{\delta}$$

$$= \frac{2N_K a_K{}^2}{9(N-1)} \sum_{j,k=1}^{N} (\delta_{i+1,j}\delta_{i+1,k} - \delta_{i,j}\delta_{i+1,k} - \delta_{i+1,j}\delta_{i,k} + \delta_{i,j}\delta_{i,k}) C_{jk} \boldsymbol{\delta}$$

$$= \frac{2N_K a_K{}^2}{9(N-1)} \sum_{\boldsymbol{j,k}=1}^{\boldsymbol{N}} (\delta_{i+1,j} - \delta_{i,j})(\delta_{i+1,k} - \delta_{i,k}) C_{jk} \boldsymbol{\delta} \qquad \text{(B17)}$$

$$= \frac{2N_K a_K{}^2}{9(N-1)} \sum_{j,k=1}^{N} \overline{B}_{ij} \overline{B}_{ik} C_{jk} \boldsymbol{\delta}$$

$$= K \frac{2N_K a_K{}^2}{9(N-1)} \boldsymbol{\delta}$$

Here, $\overline{B}_{ij} = \delta_{i+1,j} - \delta_{i,j}$, $\sum_{\nu} \overline{B}_{i,\nu} \overline{B}_{\nu,j} = A_{ij}$, and

$$K = \sum_{j,k=1}^{N} \overline{B}_{ij} \overline{B}_{ik} C_{jk} \text{ , } i=1 \ldots \ldots N\text{-}1. \qquad \text{(B18)}$$

We now use the relation

$$< \left| \boldsymbol{R}_{i+1} - \boldsymbol{R}_i \right| \left| \boldsymbol{R}_{i+1} - \boldsymbol{R}_i \right| >=< \left| s_{i+1}\boldsymbol{u}_{i+1} + \boldsymbol{P}_{i+1} - s_i \boldsymbol{u}_i - \boldsymbol{P}_i \right| \left| s_{i+1}\boldsymbol{u}_{i+1} + \boldsymbol{P}_{i+1} - s_i \boldsymbol{u}_i - \boldsymbol{P}_i \right| >$$
$$=< (s_{i+1} - s_i)(s_{i+1} - s_i) > + < \left| \boldsymbol{P}_{i+1} - \boldsymbol{P}_i \right| \left| \boldsymbol{P}_{i+1} - \boldsymbol{P}_i \right| > \qquad \text{(B19)}$$

This expression is exact when both beads are in the same tube segment, while it is only approximate when the beads are the first and last in adjacent segments. At equilibrium,

$$< \left| \boldsymbol{R}_{i+1} - \boldsymbol{R}_i \right| \left| \boldsymbol{R}_{i+1} - \boldsymbol{R}_i \right| >= \frac{N_K a_K{}^2}{N-1}, \quad \text{while} \quad < (s_{i+1} - s_i)(s_{i+1} - s_i) >= \frac{N_K a_K{}^2}{3(N-1)} + \frac{ZN_K a_K{}^2}{(N-1)^2}.$$

[The second equality follows directly from Eq. (6.71) in Doi and Edwards (1986).] Hence,

$$< \left| \boldsymbol{P}_{i+1} - \boldsymbol{P}_i \right| \left| \boldsymbol{P}_{i+1} - \boldsymbol{P}_i \right| >= \frac{2N_K a_K{}^2}{3(N-1)} - \frac{ZN_K a_K{}^2}{(N-1)^2} \qquad \text{(B20)}$$

Comparing Eqs. (B17) and (B20), K must be independent of the bead index and given by

$$K = 1 - \frac{3Z}{2(N-1)}. \tag{B21}$$

Now, Eq. (B18) comprises $N-1$ equations for the N unknown variables α_i. The tube is not stretched at equilibrium, hence the beads should be uniformly distributed around the tube centerline; i.e., the mean-square bead distance from the tube centerline, $<|\boldsymbol{P}_i\boldsymbol{P}_i|>$, must be independent of the position of the bead, *i*. Hence, from Eq. (B16), C_{ii} is a constant for all *i*, which provides the N^{th} equation. We thus obtain

$$4\lambda_H \frac{\alpha_i}{\zeta} = \begin{cases} -2 + \dfrac{2}{K} & i = 1, N \\ -4 - \dfrac{2}{K-2} + \dfrac{2}{K} & i \neq 1, N \end{cases} \tag{B22}$$

and Eq. (8) follows immediately. We assume that the harmonic potential derived using equilibrium statistics is unchanged by flow.

APPENDIX C. Algorithm

We rearrange Eqs. (B5) and (B6) by subtracting the i^{th} equation from the $(i\text{-}1)^{st}$ and replacing differentials with finite differences to obtain an Euler forward difference scheme:

$$\begin{aligned}
&\boldsymbol{Q}_1^{s}(t+\Delta t) = \boldsymbol{Q}_1{}^{s}(t) + (s_2\boldsymbol{\kappa}:\boldsymbol{u}_{t(2)}\boldsymbol{u}_{t(2)} - s_1\boldsymbol{\kappa}:\boldsymbol{u}_{t(1)}\boldsymbol{u}_{t(1)})\Delta t + \\
&\left\{\begin{matrix}\boldsymbol{u}_{t(2)}\cdot(\boldsymbol{\kappa}+\boldsymbol{\kappa}^T)\cdot\boldsymbol{P}_2 - \\ \boldsymbol{u}_{t(1)}\cdot(\boldsymbol{\kappa}+\boldsymbol{\kappa}^T)\cdot\boldsymbol{P}_1\end{matrix}\right\}\Delta t + \frac{1}{\zeta}(\boldsymbol{F}_2{}^{s} - 2\boldsymbol{F}_1{}^{s})\Delta t + \frac{1}{\zeta}\left|\boldsymbol{F}^T\right|\Delta t + \\
&\left\{(\boldsymbol{u}_{t(2),x}\xi_{2,x} + \boldsymbol{u}_{t(2),y}\xi_{2,y} + \boldsymbol{u}_{t(2),z}\xi_{2,z}) - (\boldsymbol{u}_{t(1),x}\xi_{1,x} + \boldsymbol{u}_{t(1),y}\xi_{1,y} + \boldsymbol{u}_{t(1),z}\xi_{1,z})\right\}\sqrt{\frac{2k_BT}{\zeta}}\sqrt{\Delta t}
\end{aligned} \tag{C1a}$$

$$\begin{aligned}
&\boldsymbol{Q}_{n\text{-}1}^{s}(t+\Delta t) = \boldsymbol{Q}_{n\text{-}1}{}^{s}(t) + (s_n\boldsymbol{\kappa}:\boldsymbol{u}_{t(n)}\boldsymbol{u}_{t(n)} - s_{n-1}\boldsymbol{\kappa}:\boldsymbol{u}_{t(n-1)}\boldsymbol{u}_{t(n-1)})\Delta t + \\
&\left\{\begin{matrix}\boldsymbol{u}_{t(n)}\cdot(\boldsymbol{\kappa}+\boldsymbol{\kappa}^T)\cdot\boldsymbol{P}_n - \\ \boldsymbol{u}_{t(n-1)}\cdot(\boldsymbol{\kappa}+\boldsymbol{\kappa}^T)\cdot\boldsymbol{P}_{n-1}\end{matrix}\right\}\Delta t + \frac{1}{\zeta}(\boldsymbol{F}_n{}^{s} - 2\boldsymbol{F}_{n-1}{}^{s} + \boldsymbol{F}_{n-2}{}^{s})\Delta t + \\
&\left\{\begin{matrix}(\boldsymbol{u}_{t(n),x}\xi_{n,x} + \boldsymbol{u}_{t(n),y}\xi_{n,y} + \boldsymbol{u}_{t(n),z}\xi_{n,z}) - \\ (\boldsymbol{u}_{t(n-1),x}\xi_{n-1,x} + \boldsymbol{u}_{t(n-1),y}\xi_{n-1,y} + \boldsymbol{u}_{t(n-1),z}\xi_{n-1,z})\end{matrix}\right\}\sqrt{\frac{2k_BT}{\zeta}}\sqrt{\Delta t}
\end{aligned} \tag{C1b}$$

$$\begin{aligned}
&\boldsymbol{Q}_{N-1}^{s}(t+\Delta t) = \boldsymbol{Q}_{N-1}^{s}(t) + (s_N\boldsymbol{\kappa}:\boldsymbol{u}_{t(N)}\boldsymbol{u}_{t(N)} - s_{N-1}\boldsymbol{\kappa}:\boldsymbol{u}_{t(N-1)}\boldsymbol{u}_{t(N-1)})\Delta t + \\
&\left\{\begin{matrix}\boldsymbol{u}_{t(N)}\cdot(\boldsymbol{\kappa}+\boldsymbol{\kappa}^T)\cdot\boldsymbol{P}_N - \\ \boldsymbol{u}_{t(N-1)})\cdot(\boldsymbol{\kappa}+\boldsymbol{\kappa}^T)\cdot\boldsymbol{P}_{N-1}\end{matrix}\right\}\Delta t + \frac{1}{\zeta}(-2\boldsymbol{F}_{N-1}^{s} + \boldsymbol{F}_{N-2}^{s})\Delta t + \frac{1}{\zeta}\left|\boldsymbol{F}^T\right|\Delta t + \\
&\left\{\begin{matrix}(\boldsymbol{u}_{t(N),x}\xi_{N,x} + \boldsymbol{u}_{t(N),y}\xi_{N,y} + \boldsymbol{u}_{t(N),z}\xi_{N,z}) - \\ (\boldsymbol{u}_{t(N-1),x}\xi_{N-1,x} + \boldsymbol{u}_{t(N-1),y}\xi_{N-1,y} + \boldsymbol{u}_{t(N-1),z}\xi_{N-1,z})\end{matrix}\right\}\sqrt{\frac{2k_BT}{\zeta}}\sqrt{\Delta t}
\end{aligned} \tag{C1c}$$

$$s_M(t+\Delta t) = s_M(t) + s_M \boldsymbol{\kappa} : \boldsymbol{u}_{t(M)}\boldsymbol{u}_{t(M)}\Delta t + \boldsymbol{u}_{t(M)} \cdot (\boldsymbol{\kappa} + \boldsymbol{\kappa}^T) \cdot \boldsymbol{P}_M \Delta t + \frac{1}{\zeta}(\boldsymbol{F}_M{}^s - \boldsymbol{F}_{M-1}{}^s)\Delta t + (\boldsymbol{u}_{t(M),x}\xi_{M,x} + \boldsymbol{u}_{t(M),y}\xi_{M,y} + \boldsymbol{u}_{t(M),z}\xi_{M,z})\sqrt{\frac{2k_BT}{\zeta}}\sqrt{\Delta t} \tag{C1d}$$

$$\boldsymbol{Q}_1{}^{P_q}(t+\Delta t) = \boldsymbol{Q}_1{}^{P_q}(t) + \left\{(\boldsymbol{\kappa}\cdot\boldsymbol{P}_2)_q - (\boldsymbol{\kappa}\cdot\boldsymbol{P}_1)_q\right\}\Delta t - \begin{Bmatrix} \boldsymbol{u}_{t(2),q}\boldsymbol{u}_{t(2)} \cdot (\boldsymbol{\kappa}+\boldsymbol{\kappa}^T)\cdot\boldsymbol{P}_2 - \\ \boldsymbol{u}_{t(1),q}\boldsymbol{u}_{t(1)} \cdot (\boldsymbol{\kappa}+\boldsymbol{\kappa}^T)\cdot\boldsymbol{P}_1 \end{Bmatrix}\Delta t + \frac{1}{\zeta}(\boldsymbol{F}_2{}^{P_q} - 2\boldsymbol{F}_1{}^{P_q})\Delta t - \frac{1}{\zeta}(\alpha_2\boldsymbol{P}_{2,q} - \alpha_1\boldsymbol{P}_{1,q})\Delta t + \begin{Bmatrix} (\xi_{2,q} - (\xi_{2,x}\boldsymbol{u}_{t(2),x} + \xi_{2,y}\boldsymbol{u}_{t(2),y} + \xi_{2,z}\boldsymbol{u}_{t(2),z})\boldsymbol{u}_{t(2),q}) - \\ (\xi_{1,q} - (\xi_{1,x}\boldsymbol{u}_{t(1),x} + \xi_{1,y}\boldsymbol{u}_{t(1),y} + \xi_{1,z}\boldsymbol{u}_{t(1),z})\boldsymbol{u}_{t(1),q}) \end{Bmatrix}\sqrt{\frac{2k_BT}{\zeta}}\sqrt{\Delta t} \tag{C1e}$$

$$\boldsymbol{Q}_{n\text{-}1}{}^{P_q}(t+\Delta t) = \boldsymbol{Q}_{n\text{-}1}{}^{P_q}(t) + \left\{(\boldsymbol{\kappa}\cdot\boldsymbol{P}_n)_q - (\boldsymbol{\kappa}\cdot\boldsymbol{P}_{n-1})_q\right\}\Delta t - \begin{Bmatrix} \boldsymbol{u}_{t(n),q}\boldsymbol{u}_{t(n)} \cdot (\boldsymbol{\kappa}+\boldsymbol{\kappa}^T)\cdot\boldsymbol{P}_n - \\ \boldsymbol{u}_{t(n-1),q}\boldsymbol{u}_{t(n-1)} \cdot (\boldsymbol{\kappa}+\boldsymbol{\kappa}^T)\cdot\boldsymbol{P}_{n-1} \end{Bmatrix}\Delta t + \frac{1}{\zeta}(\boldsymbol{F}_n{}^{P_q} - 2\boldsymbol{F}_{n-1}{}^{P_q} + \boldsymbol{F}_{n-2}{}^{P_q})\Delta t - \frac{1}{\zeta}(\alpha_n\boldsymbol{P}_{n,q} - \alpha_{n-1}\boldsymbol{P}_{n-1,q})\Delta t + \begin{Bmatrix} (\xi_{n,q} - (\xi_{n,x}\boldsymbol{u}_{t(n),x} + \xi_{n,y}\boldsymbol{u}_{t(n),y} + \xi_{n,z}\boldsymbol{u}_{t(n),z})\boldsymbol{u}_{t(n),q}) - \\ (\xi_{n-1,q} - (\xi_{n-1,x}\boldsymbol{u}_{t(n-1),x} + \xi_{n-1,y}\boldsymbol{u}_{t(n-1),y} + \xi_{n-1,z}\boldsymbol{u}_{t(n-1),z})\boldsymbol{u}_{t(n-1),q}) \end{Bmatrix}\sqrt{\frac{2k_BT}{\zeta}}\sqrt{\Delta t} \tag{C1f}$$

$$\boldsymbol{Q}_{N-1}{}^{P_q}(t+\Delta t) = \boldsymbol{Q}_{N-1}{}^{P_q}(t) + \left\{(\boldsymbol{\kappa}\cdot\boldsymbol{P}_N)_q - (\boldsymbol{\kappa}\cdot\boldsymbol{P}_{N-1})_q\right\}\Delta t - \begin{Bmatrix} \boldsymbol{u}_{t(N),q}\boldsymbol{u}_{t(N)} \cdot (\boldsymbol{\kappa}+\boldsymbol{\kappa}^T)\cdot\boldsymbol{P}_N - \\ \boldsymbol{u}_{t(N-1),q}\boldsymbol{u}_{t(N-1)} \cdot (\boldsymbol{\kappa}+\boldsymbol{\kappa}^T)\cdot\boldsymbol{P}_{N-1} \end{Bmatrix}\Delta t + \frac{1}{\zeta}(-2\boldsymbol{F}_{N-1}{}^{P_q} + \boldsymbol{F}_{N-2}{}^{P_q})\Delta t - \frac{1}{\zeta}(\alpha_N\boldsymbol{P}_{N,q} - \alpha_{N-1}\boldsymbol{P}_{N-1,q})\Delta t + \begin{Bmatrix} (\xi_{N,q} - (\xi_{N,x}\boldsymbol{u}_{t(N),x} + \xi_{N,y}\boldsymbol{u}_{t(N),y} + \xi_{N,z}\boldsymbol{u}_{t(N),z})\boldsymbol{u}_{t(N),q}) - \\ (\xi_{N-1,q} - (\xi_{N-1,x}\boldsymbol{u}_{t(N-1),x} + \xi_{N-1,y}\boldsymbol{u}_{t(N-1),y} + \xi_{N-1,z}\boldsymbol{u}_{t(N-1),z})\boldsymbol{u}_{t(N-1),q}) \end{Bmatrix}\sqrt{\frac{2k_BT}{\zeta}}\sqrt{\Delta t} \tag{C1g}$$

$$\boldsymbol{P}_M{}^q(t+\Delta t) = \boldsymbol{P}_M{}^q(t) + (\boldsymbol{\kappa}\cdot\boldsymbol{P}_M)_q\Delta t - \boldsymbol{u}_{t(M),q}\boldsymbol{u}_{\boldsymbol{t(M)}}\cdot(\boldsymbol{\kappa}+\boldsymbol{\kappa}^T)\cdot\boldsymbol{P}_M\Delta t$$
$$+\frac{1}{\zeta}(\boldsymbol{F}_M{}^{\boldsymbol{P}_q} - \boldsymbol{F}_{M-1}{}^{\boldsymbol{P}_q})\Delta t - \frac{1}{\zeta}\alpha_M\boldsymbol{P}_{M,q}\Delta t + \qquad \text{(C1h)}$$
$$(\xi_{M,q} - (\xi_{M,x}\boldsymbol{u}_{t(M),x} + \xi_{M,y}\boldsymbol{u}_{t(M),y} + \xi_{M,z}\boldsymbol{u}_{t(M),z})\boldsymbol{u}_{t(M),q})\sqrt{\frac{2k_BT}{\zeta}}\sqrt{\Delta t}$$

$n = 2,3.....N-2$, $q = x, y, z$

Here, $\boldsymbol{Q}_i^{\,s} = s_{i+1} - s_i$, $Q_i^{\,\boldsymbol{P_q}} = \boldsymbol{P}_{i+1,q} - \boldsymbol{P}_{i,q}$, $\boldsymbol{F}_i^{\,s} = \dfrac{H(s_{i+1}-s_i)}{1-\dfrac{\left|\boldsymbol{R}_{i+1}-\boldsymbol{R}_i\right|^2}{b^2}}$, and $\boldsymbol{F}_i^{\,\boldsymbol{P_q}} = \dfrac{H(\boldsymbol{P}_{i+1,q}-\boldsymbol{P}_{i,q})}{1-\dfrac{\left|R_{i+1}-R_i\right|^2}{b^2}}$.

$\xi_{i,q}$ is a random number with zero mean and unit variance, and the Mth bead is located in the middle of the chain.

The simulation is started at equilibrium. (Equilibration is established by checking that transients initiated after different equilibration times give the same result.) The dimensionless time step size is chosen to be 0.01; a smaller time step size has no impact on the results. At each time step the stochastic equations (C1) are integrated and the tube segments are moved affinely according to Eq. (10). The tube segments are then rearranged (cut, changed in length, new segment added), as appropriate, after which constraints are released and new constraints are formed. The stress is calculated from Eq. (11) and the process is repeated.

Appendix D. Summary of procedures of the bulk simulation

In flowchart D1, we summarize the procedures for our bulk simulation. The specific simulation algorithm used in the steps that are marked with * is shown in flowchart 2.

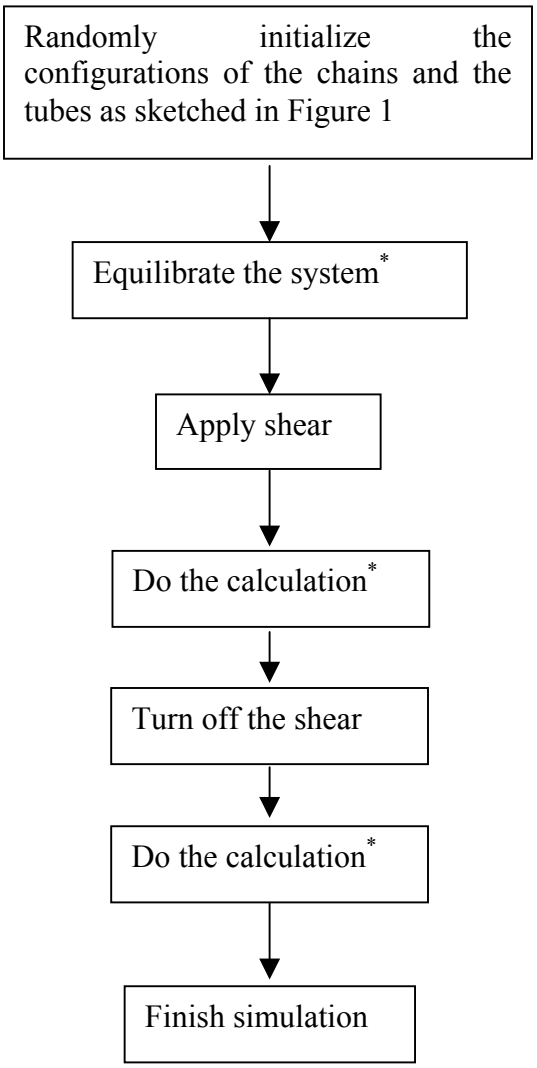

Flowchart D1 Procedures of the simulation. The algorithm used in the steps marked with * is shown in flowchart D2.

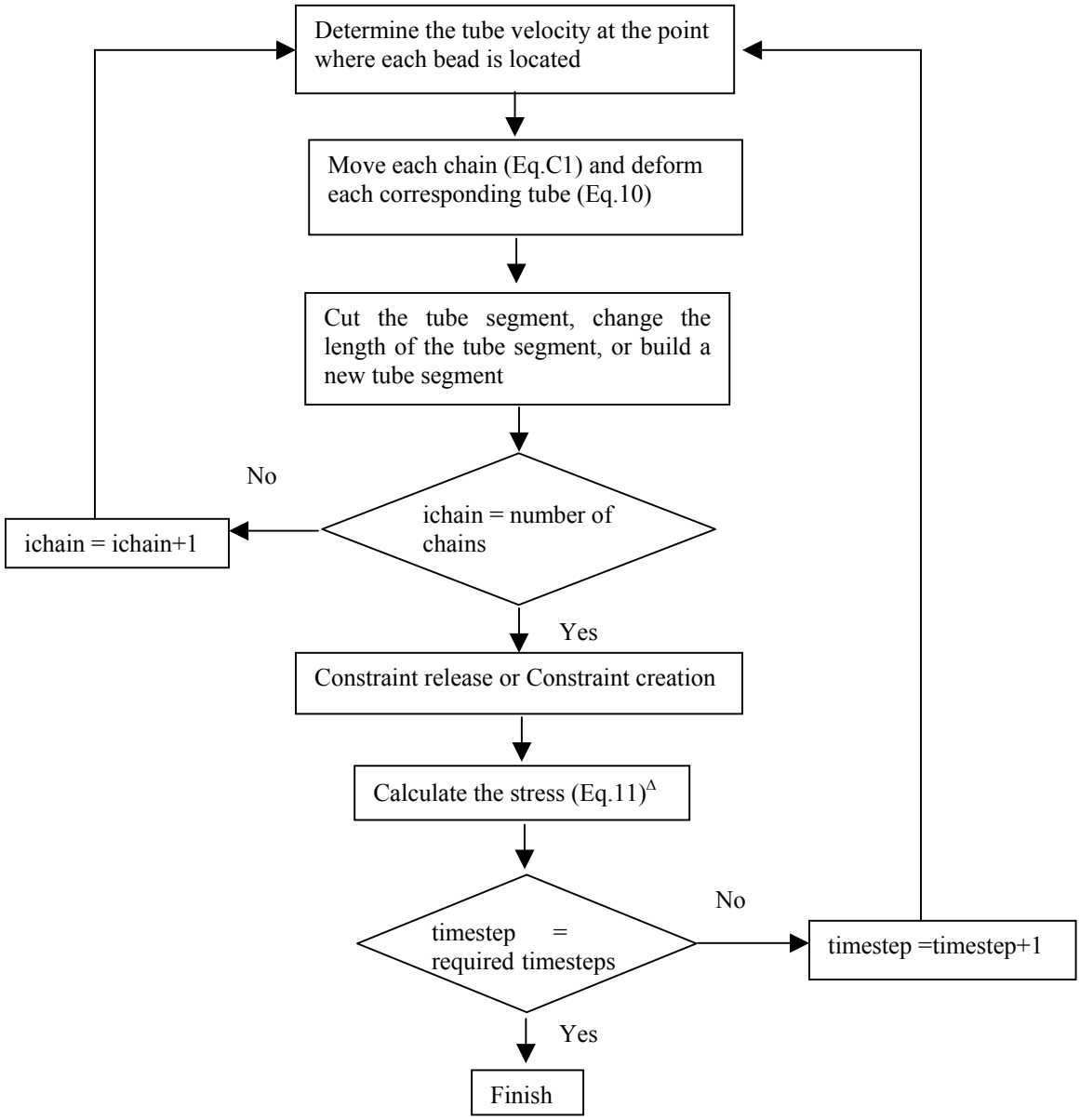

Flowchart D2 Simulation algorithm for the marked steps in flowchart 1. $^{\Delta}$ This step is not needed for equilibrating the system.

APPENDIX E Impact of the averaging interval Λ on G(t)

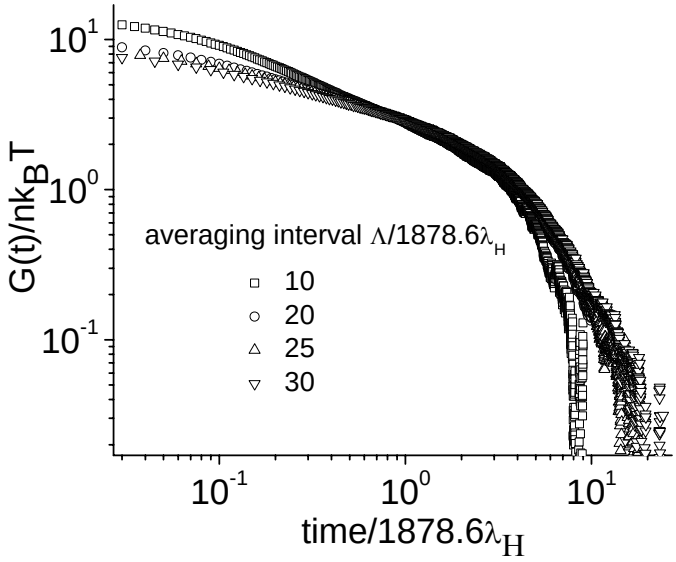

Fig. E1 G(t) obtained from different averaging intervals Λ for 13 volume % tricresyl phosphate solution of polystyrene with a molecular weight of 1.9×10^6 and a polydispersity of 1.2. The corresponding tube segment number z = 9 and beads number N = 37.

Fig E1 shows that the simulated G(t) converges as the averaging interval Λ increases in Eq. (13).

APPENDIX F. Impact of the time step

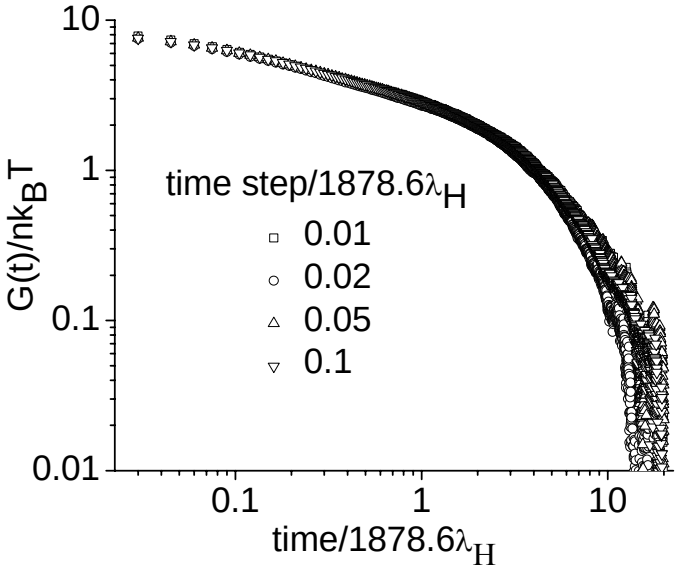

Fig. F1 Relaxation modulus G(t) computed from the Green-Kubo equation with time steps 0.01, 0.02, 0.05 and $0.1\times1878.6\lambda_H$ for 13 volume % tricresyl phosphate solution of polystyrene with a molecular weight of 1.9×10^6 and a polydispersity of 1.2. The corresponding tube segment number Z = 9 and beads number N = 37.

In Fig. F1, the investigated time steps give almost the identical results at short time. The deviation only occurs at long times when the time step is larger than $0.02\times1878.6\boldsymbol{\lambda_H}$.

APPENDIX G. **Effect of coarse graining on the prediction of the linear viscoselastic properties**

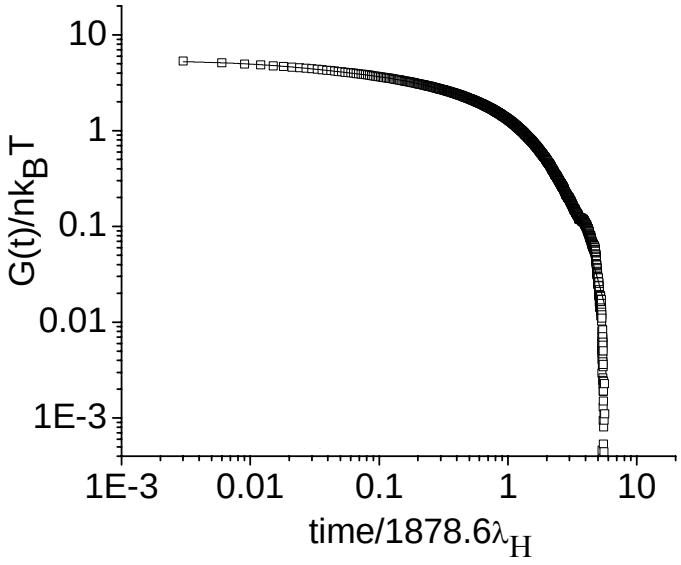

Fig. G1 Relaxation modulus G(t) computed from the Green-Kubo equation with time steps $0.01\times1878.6\lambda_H$ for 13 volume % tricresyl phosphate solution of polystyrene with a molecular weight of 1.9×10^6 and a polydispersity of 1.2; Z = 9 and N = 19.

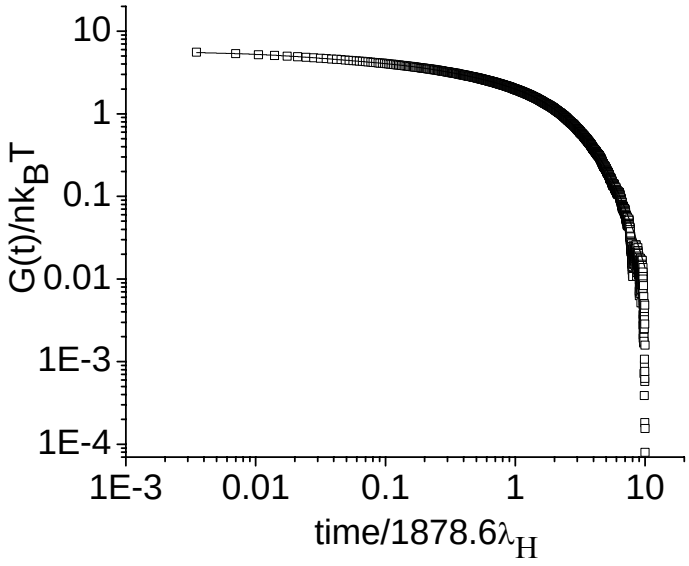

Fig. G2 Relaxation modulus G(t) computed from the Green-Kubo equation with time steps $0.01\times1878.6\lambda_H$ for 13 volume % tricresyl phosphate solution of polystyrene with a molecular weight of 1.9×10^6 and a polydispersity of 1.2; Z= 9 and N = 28

Table G1 Relaxation spectrum fitted to G(t) in Fig. G1

Weight factor g_i/nk_BT	Standard error	Time constant $\lambda_i/1878.6\lambda_H$	Standard error
3.430	±0.006	1.035	±0.001
1.036	±0.015	0.151	±0.003
0.924	±0.018	0.022	±0.001

Table G2 Relaxation spectrum fitted to G(t) in Fig. G2

Weight factor g_i/nk_BT	Standard error	Time constant $\lambda_i / 1878.6\lambda_H$	Standard error
3.455	±0.002	1.802	±0.001
1.272	±0.006	0.200	±0.001
0.941	±0.010	0.022	±0.0004

λ_H was obtained as $\lambda_H = 7.9\times10^{-3}$ s, and 4.5×10^{-3} s for N=19 and N=28, respectively. The storage and loss moduli can be computed as $G'(\omega) = nk_BT\sum_i \frac{g_i(\lambda_i\omega)^2}{1+(\lambda_i\omega)^2}$ and $G''(\omega) = nk_BT\sum_i \frac{g_i\lambda_i\omega}{1+(\lambda_i\omega)^2}$, respectively.

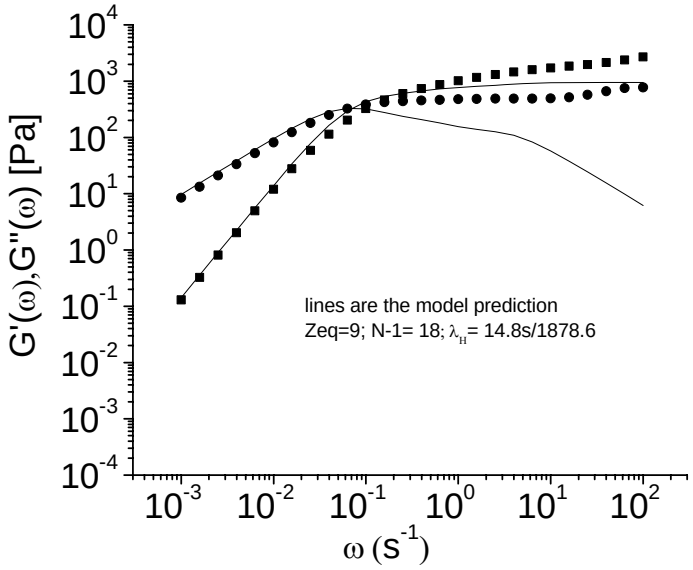

Fig. G3 G' (■) and G" (●) data of Venerus and Kahvand. The lines are computed from the model with Z = 9 and N = 19 using the spectrum in Table G1.

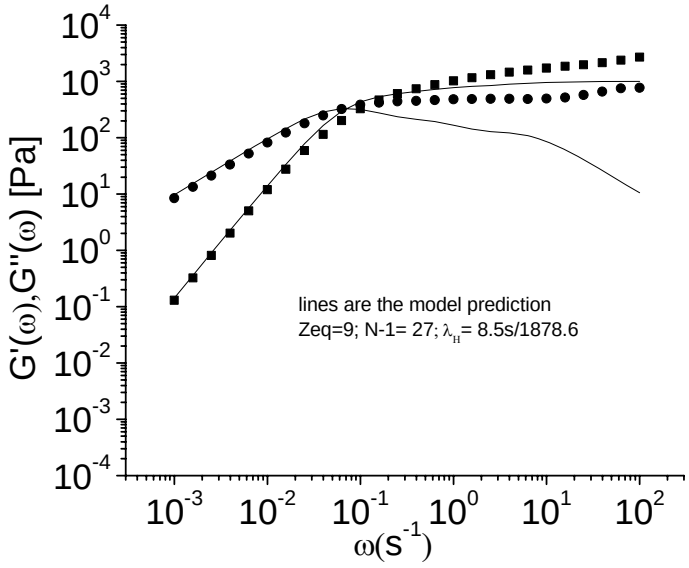

Fig G4 G' (■) and G" (●) data of Venerus and Kahvand. The lines are computed from the model with Z = 9 and N = 28 using the spectrum in Table G2.

Figs. G3 and G4, together with Fig. 2b, show that the prediction of the linear viscoelastic properties G' and G" in the terminal region is improved with an increase in the bead number used in the simulation.

APPENDIX H Agreement with Cox-Merz rule

Small Amplitude Oscillatory Shear (SAOS), whose shear rate function $\dot{\gamma}(t)$ is a cosine function shown in Eq. H1, widely used to characterize complex fluids:

$$\dot{\gamma}(t) = \dot{\gamma}_0 \cos \omega t \qquad \text{H1}$$

where $\dot{\gamma}_0$ is the constant amplitude of the shear rate and ω is the frequency. The applied strain can be calculated by the following equation,

$$\gamma(0,t) = \int_0^t \dot{\gamma}(t')dt' = \int_0^t \dot{\gamma}_0 \cos \omega t' dt' = \gamma_0 \sin \omega t \qquad \text{H2}$$

with the strain amplitude $\gamma_0 = \frac{\dot{\gamma}_0}{\omega}$.When the sample is subjected to a small enough strain amplitude, the response shear stress will be a sine wave of the same frequency ω, but not in phase with the input strain. The shear stress can be written in the following form:

$$-\boldsymbol{\tau}_{xy}(t) = \tau_0 \sin(\omega t + \delta) \qquad \text{H3}$$

where δ gives the phase difference between the strain wave and the stress response. The material functions of SAOS, the storage modulus $G'(\omega)$ and the loss modulus $G''(\omega)$, are then defined as follows, after Eq. H3 is expanded according to trigonometric identities and divided by γ_0.

$$\frac{-\boldsymbol{\tau}_{xy}}{\gamma_0} = G' \sin \omega t + G'' \cos \omega t \qquad \text{H4}$$

$$G' \equiv \frac{\tau_0}{\gamma_0} \cos \delta \qquad \text{H5}$$

$$G'' \equiv \frac{\tau_0}{\gamma_0} \sin \delta \qquad \text{H6}$$

The complex modulus is defined as

$$G^*(\omega) = G' + iG'' \qquad \text{H7}$$

The complex viscosity η^* is defined as follows:

$$\eta^*(\omega) \equiv \frac{-\tau_{xy}(t)}{\dot{\gamma}(t)} = \frac{G^*}{i\omega} = \eta' - i\eta'' \qquad \text{H8}$$

The magnitudes of the complex quantities in Eqs. H7 and H8 are

$$|G^*| = \sqrt{G'^2 + G''^2} \qquad \text{H9}$$

$$|\eta^*| = \sqrt{\eta'^2 + \eta''^2} = \frac{1}{\omega}\sqrt{G'^2 + G''^2} \qquad \text{H10}$$

It has been observed that for many materials, the steady-state-shear-viscosity versus shear rate curve coincides with the curve of the magnitude of the complex-viscosity versus frequency curve if they are compared at $\dot{\gamma}(s^{-1}) = \omega(rad/s)$; this is known as Cox-Merz rule,

$$\eta(\dot{\gamma}) = |\eta^*(\omega)|_{\dot{\gamma}=\omega} \qquad \text{H11}$$

In Figs. H1 and H2, we check the validity of the empirical Cox-Merz rule in our simulation. $|\eta^*|$ is calculated based on Eq. H10, where G' and G'' are fitted from simulated $G(t)$ described in Section 1.3 according to Eqs. H1 and H2.

$$G'(\omega) = \sum_i \frac{g_i(\lambda_i\omega)^2}{1+(\lambda_i\omega)^2} \qquad \text{H12}$$

$$G''(\omega) = \sum_i \frac{g_i\lambda_i\omega}{1+(\lambda_i\omega)^2} \qquad \text{H13}$$

We found that the model prediction does show consistency with the Cox-Merz rule within a factor of 2, although the model overpredicts shear shinning for Oberhauser and

coworkers' data. A small difference between $\eta(\dot{\gamma})$ and $|\eta^*(\omega)|$ at intermediate frequencies (shear rates) is also observed in Venerus and co-workers' experiments.

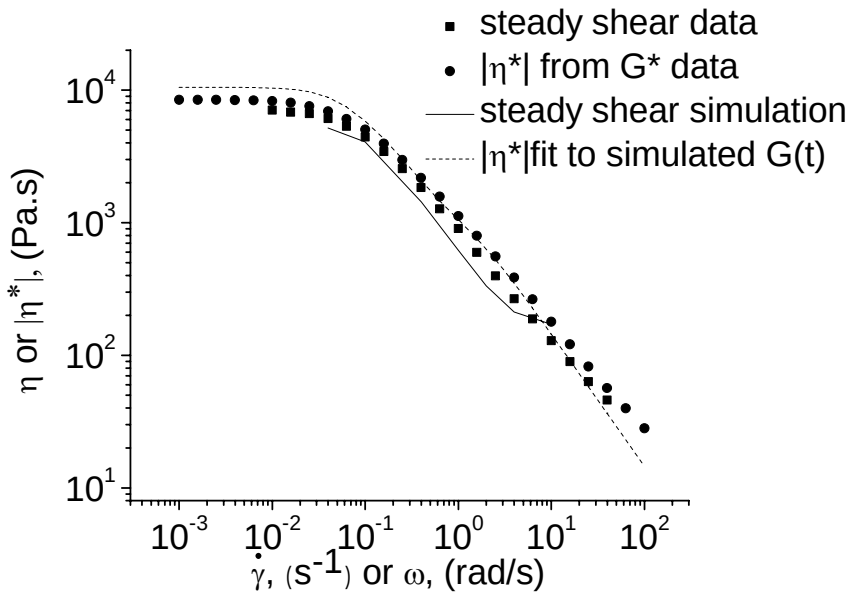

Fig. H1 Check of the Cox-Merz rule for Venerus and co-workers' data. Dots are the experimental data and the lines are predicted by the model.

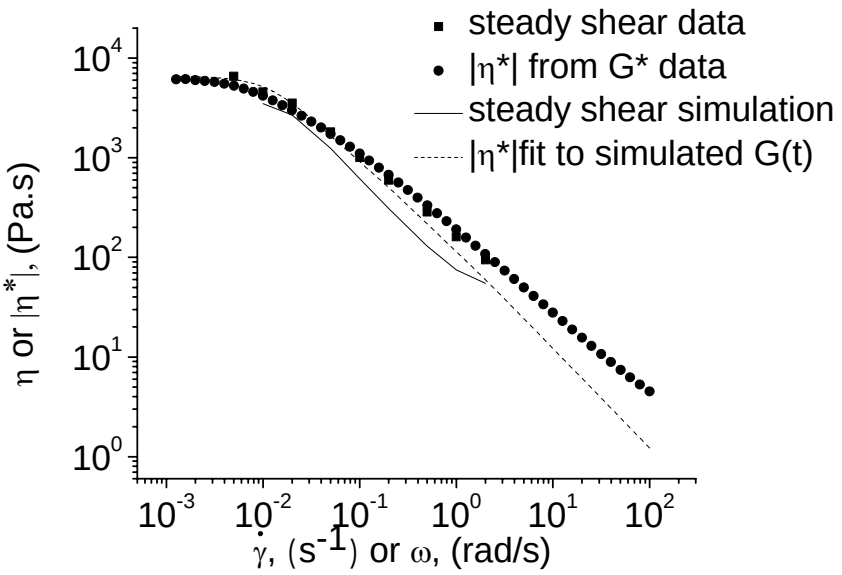

Fig. H2 Check of the Cox-Merz rule for Oberhauser and co-workers' data. Dots are the experimental data and the lines are predicted by the model.

APPENDIX I Flowchart of the simulation with the tethered chains

Step 1:

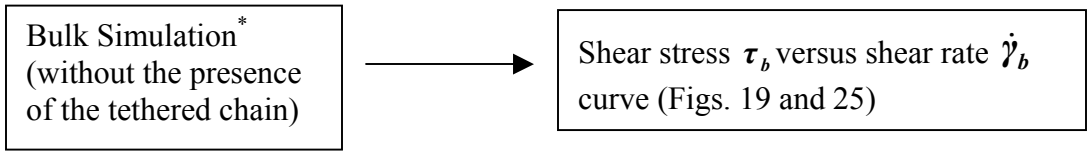

* Procedures of the bulk simulation are explained in Flowchart D1 and D2.

Step 2:

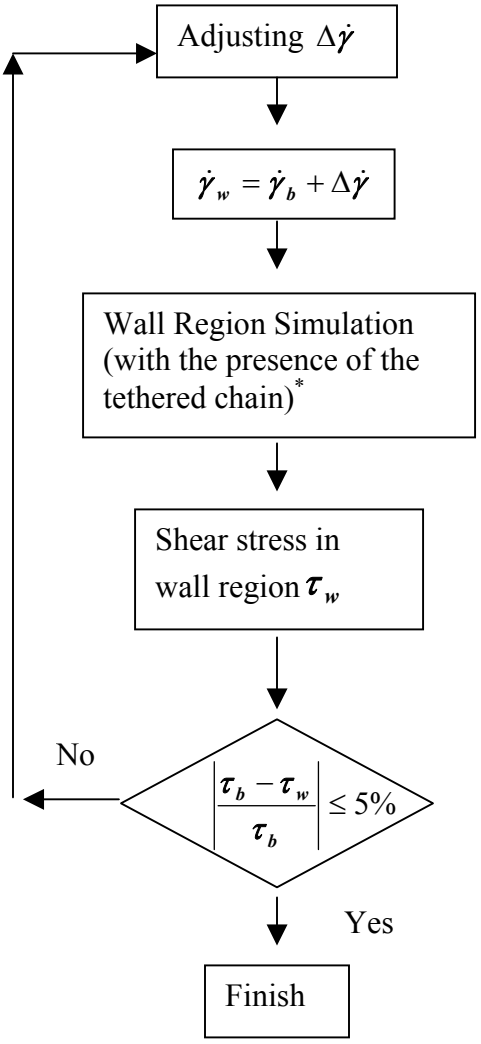

* the tethered chains and the untethered chains in the wall region are subjected to $\dot{\gamma}_w$; and the untethered chains outside the wall region are subjected to $\dot{\gamma}_b$.

Flowchart I1 Procedures of the simulation with the presence of the tethered chains

APPENDIX J Computation Errors

Since the simulation of the interaction of the tethered and untethered chains is carried out by adjusting the shear rate in the wall region, $\dot{\gamma}_w$, in order to establish a continuous shear stress in the whole domain, computational errors cannot be avoided, but they are controlled within a certain range as shown in Flowchart I1. In Tables J1, J2, J3 and J4, those errors are listed. The shear stress in the wall region, τ_w, is determined both by time averaging and by ensemble averaging after the system reaches steady state. The maximum relative error in the stress in all cases is 4.9%, and in most cases the relative error is less than 2%.

Table J1 computation errors for PDMS data

$\dot{\gamma}_b$ (s^{-1})	$\Delta\dot{\gamma}$ (s^{-1})	$\dot{\gamma}_w$ (s^{-1})	τ_b (Pa)	τ_w (Pa)	Error $\equiv \left\lvert \frac{\tau_b - \tau_w}{\tau_b} \right\rvert$
0.5	6.66667	7.16667	14670.30	15036.15	0.02494
0.83333	16.66667	17.5	24450.50	24109.20	0.01396
1.33333	66.66667	68	38807.83	38574.72	0.00601
1.66667	333.3333	335	42641.67	44409.29	0.04145
5	150000	150005	68879.99	67380.92	0.02176
8.33333	181666.7	181675	69067.77	72475.51	0.04934
3.33333	116666.7	116670	63155.84	61144.48	0.03185
2	13333.33	13335.33	47836.91	47808.99	5.84E-04
2.5	66666.67	66669.17	55682.59	54161.39	0.02732
3	116666.7	116669.7	62157.47	61577.85	0.00933
1.7	500	501.7	44093.52	43519.21	0.01302
1.8	3333.333	3335.133	45864.12	46015.26	0.0033
1.85	5000	5001.85	46716.07	46416.75	0.00641
1.9	8333.333	8335.233	47546.23	47060.86	0.01021
1.75	833.3333	835.0833	44990.05	45125.32	0.00301

Table J2 Computation errors for polybutadiene data with grafted chain molecular weight 67,300

$\dot{\gamma}_b$ (s^{-1})	$\Delta\dot{\gamma}$ (s^{-1})	$\dot{\gamma}_w$ (s^{-1})	τ_b (Pa)	τ_w (Pa)	Error $\equiv \left\lvert \frac{\tau_b - \tau_w}{\tau_b} \right\rvert$
21.92982	1147.661	1169.591	121398.5	122428.9	0.00849
29.23977	20438.6	20467.84	156909.6	153371.9	0.02255
36.54971	30665.2	30701.75	185814.0	190687.0	0.02623
43.85965	35043.86	35087.72	209350.4	215915.6	0.03136
51.16959	43808.48	43859.65	237016.1	234634.8	0.01005
58.47953	46725.15	46783.63	263443.0	255086.2	0.03172

Table J3 Computation errors for polybutadiene data with grafted chain molecular weight 32,600

$\dot{\gamma}_b$ (s^{-1})	$\Delta\dot{\gamma}$ (s^{-1})	$\dot{\gamma}_w$ (s^{-1})	τ_b (Pa)	τ_w (Pa)	Error $\equiv \left\lvert \frac{\tau_b - \tau_w}{\tau_b} \right\rvert$
21.92982	21907.89	21929.82	121398.5	119962.2	0.01183
29.23977	62836.26	62865.5	156909.6	153481.5	0.02185
36.54971	84027.78	84064.33	185814.0	184588.9	0.00659
43.85965	103026.3	103070.2	209350.4.0	209173.3	8.46E-04
51.16959	116907.9	116959.1	237016.1	231047.2	0.02518
58.47953	131520.5	131578.9	263443.0	254340.7	0.03455

Table J4 Computation errors for polybutadiene data with grafted chain molecular weight 15,200

$\dot{\gamma}_b$ (s^{-1})	$\Delta\dot{\gamma}$ (s^{-1})	$\dot{\gamma}_w$ (s^{-1})	τ_b (Pa)	τ_w (Pa)	Error $\equiv \left\lvert \frac{\tau_b - \tau_w}{\tau_b} \right\rvert$
21.92982	131557	131578.9	121398.5	120480.2	0.00756
29.23977	197339.2	197368.4	156909.6	156222.2	0.00438
36.54971	248501.5	248538	185814.0	186205.9	0.00211
43.85965	292353.8	292397.7	209350.4	211672.9	0.01109
51.16959	343516.1	343567.3	237016.1	245570.4	0.03609
58.47953	387368.4	387426.9	263443.0	271881.5	0.03203

APPENDIX K Impact of the definition of the thickness of the wall region

The apparent slip velocity and the slip length are dependent on the choice of the thickness of the wall region. Another possible definition of the thickness of the wall region, different from what is used in chapter 2, is discussed in this appendix. In our model, the chain segment between the point of tethering and the first entanglement is assumed to be free of the tube; in other words, that part of the chain disentangles from the surrounding chains. So it is also meaningful to extrapolate the bulk velocity to the wall, using the velocity at the end of the first entanglement as the initial value, and the corresponding thickness of the wall region to be the average height of the first entanglement, in the shear direction, as shown in Fig. K1. The definition of the slip length remains the same, but the value changes due to the different position of the edge of the wall region.

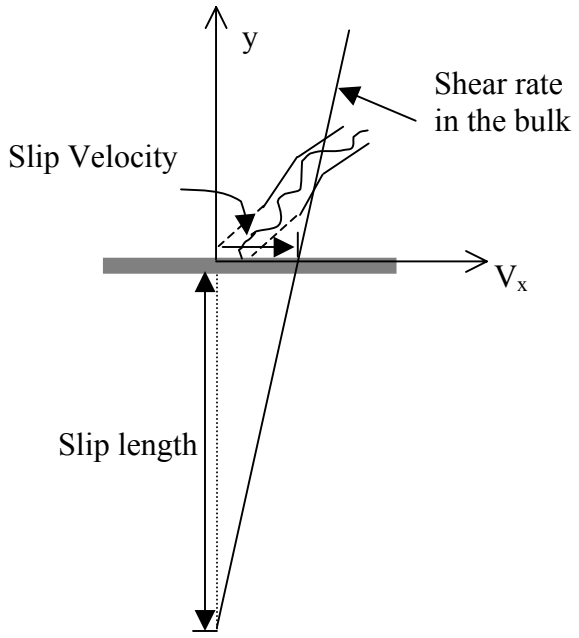

Fig K1 Another definition of the slip velocity and slip length

In Figs. K2 and K3, we compare the shear rate in the bulk versus slip velocity curve and slip velocity versus slip length curve (PDMS data) resulting from two definitions of the thickness of the wall region. Two definitions give a difference of abound a factor of 5 times in the slip velocity at a specified shear rate in the bulk. In fact, Figs K4 and Fig.22 clearly show that the thickness of the wall region directly contributes to the factor of 5. The definition does not change the slip velocity versus slip length curve significantly before the curve reaches the plateau because the thickness of the wall region has the same impact on the slip velocity and slip length. From the experimental point of view, the wall region that can be probed is usually much thicker than values shown in Fig. K4 because of the limited experimental penetration depth (e.g. Durliat and coworkers(1997) show the penetration depth of the order of 75nm.)

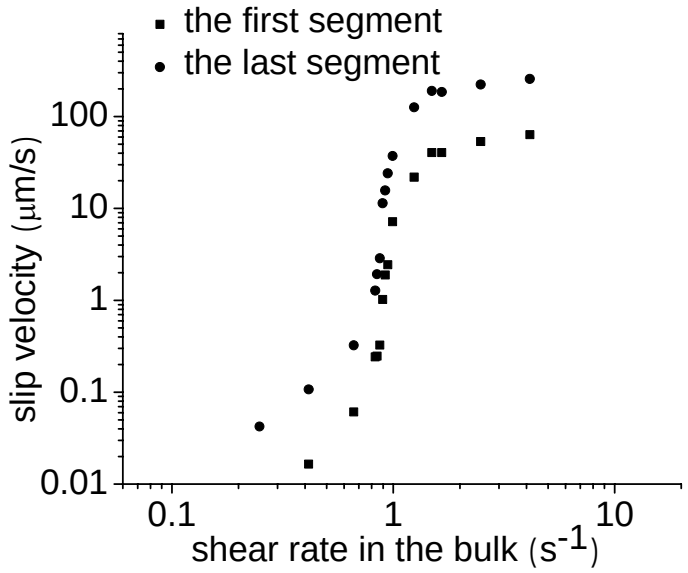

Fig. K2 Comparison of the slip velocity versus shear rate in the bulk for two definitions of the thickness of the wall region (PDMS data). The square is the result of the slip velocity being taken to be the velocity at the edge of the last entanglement on the tethered chain; the circle is the result of the slip velocity being taken to be the velocity at the end of the first entanglement on the tethered chain.

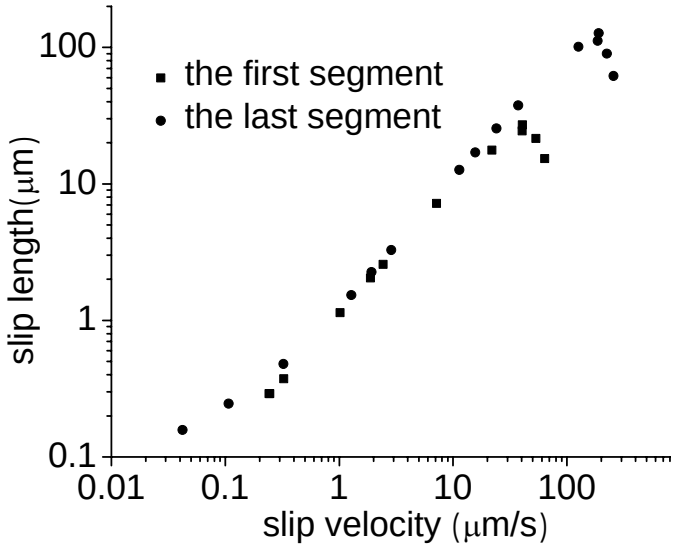

Fig. K3 Comparison of slip length versus slip velocity for two definitions of the thickness of the wall region (PDMS data). The square is the result of the slip velocity being taken to be the velocity at the edge of the last entanglement on the tethered chain; the circle is the result of the slip velocity being taken to be the velocity at the end of the first entanglement on the tethered chain.

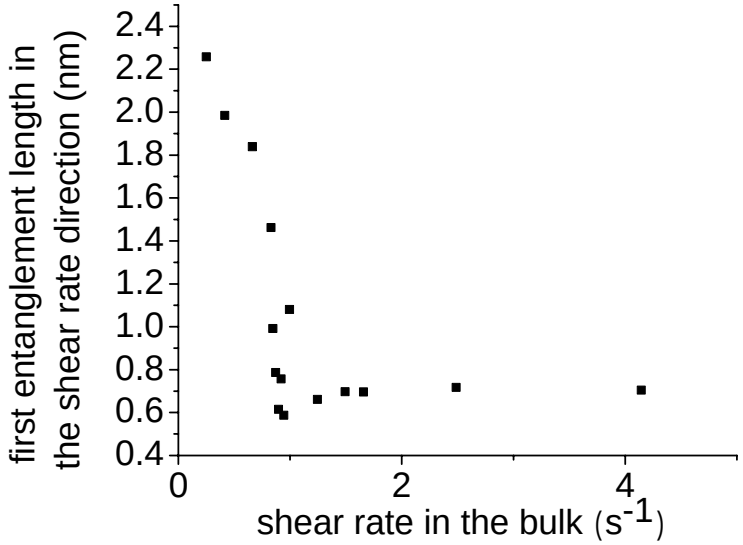

Fig. K4 Length of the first entanglement on the tethered chain in the shear rate direction as a function of the shear rate in the bulk (PDMS data).

In Figs.K5 and K6, we show a vertical shift by about a factor of 3 compared with the results in Figs. 26 and 27. The corresponding change of the thickness of the wall region is demonstrated in Figs. K7 and K8. With the exception of one point, the length of the first entanglement on the tethered chain or the total tethered chain in the shear rate direction is within the plateau region in the stress range considered.

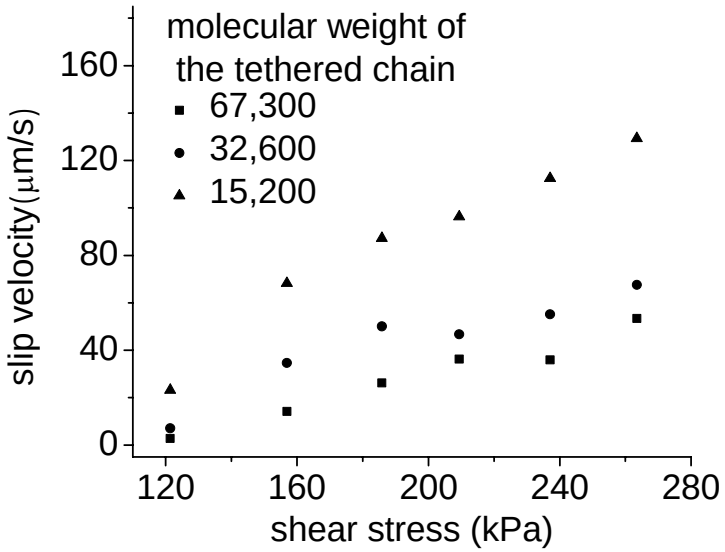

Fig. K5 Calculated slip velocity as a function of shear stress for different surface chain molecular weights with the thickness of the wall region taken as the end of the first entanglement on the tethered chain (PBDE data).

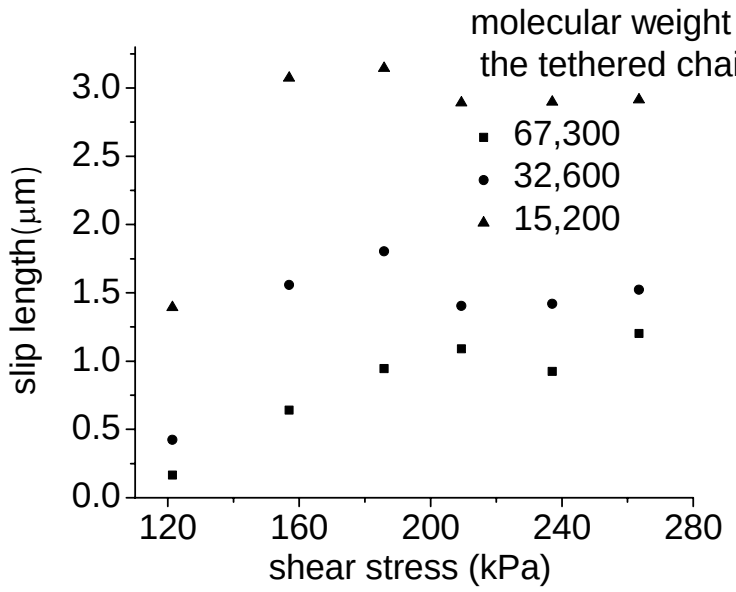

Fig. K6 Calculated slip length as a function of shear stress for different surface chain molecular weights with the thickness of the wall region taken as the end of the first entanglement on the tethered chain (PBDE data).

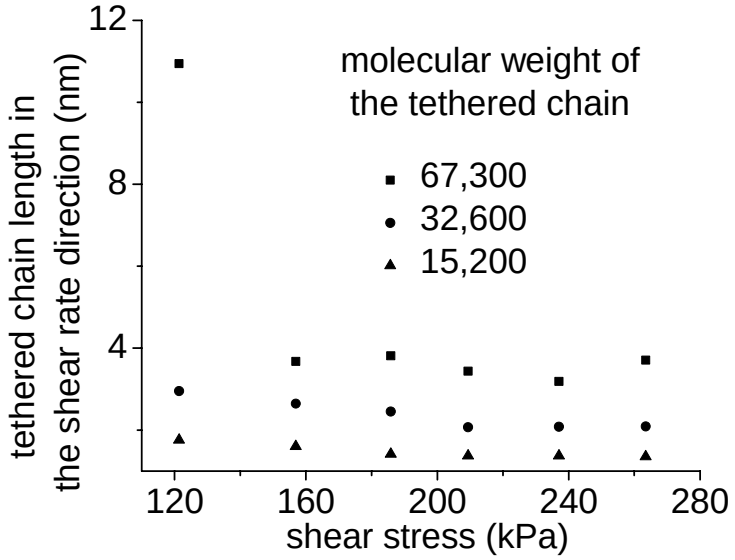

Fig. K7 Length of the tethered chain in the shear rate direction as a function of the shear rate in the bulk (PBDE data).

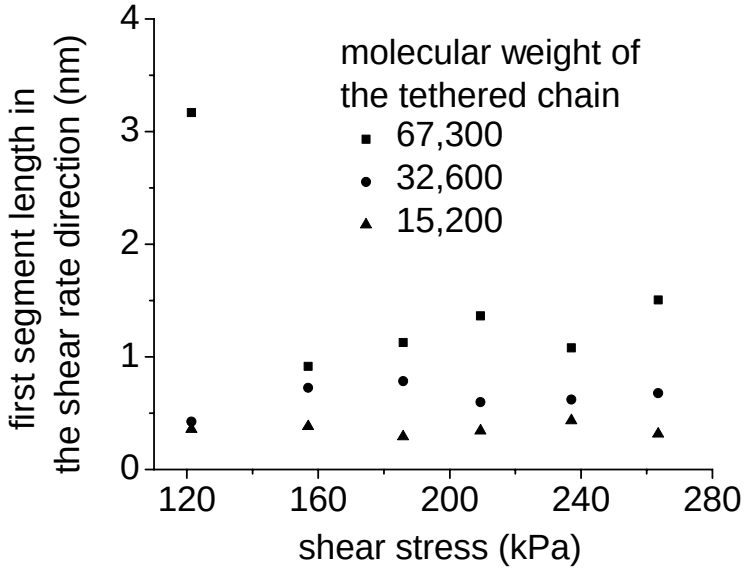

Fig. K8 Length of the first entanglement on the tethered chain in the shear rate direction as a function of the shear rate in the bulk (PBDE data).

Bibliography:

Benbow, J. J. and P. Lamb, "New aspects of melt fracture," SPE Trans. **3**, 7-17 (1963).

Bercea, M., C. Peiti, B. Simionescu and P. Navard, "Shear rheology of semidilute poly(methyl methacrylate) solution," Macromolecules **26**, 7095-7096 (1993).

Bergem, N. (1976). "Visualization studies of polymer melt flow anomalies in extrusion". Proc. Int. Congr. Rheol., 7th, Gothenburg, Sweden, Swed. Soc. Rheol.

Bird, R. B., R. C. Armstrong and O. Hassager. *Dynamics of polymeric liquids*.(Wiley,New York,1987)

Birshtein, T. M. and O. B. Ptitsyn. *Conformations of macromolecules*.(Interscience,New York,1966)

Brochard, F., B. Gay and P.-G. d. Gennes, "Slippage of polymer melts on grafted surfaces," Mcromolecules **29**, 377-382 (1996).

Brochard-Wyart, F. and P.-G. d. Gennes, "Shear-dependent slippage at a polymer/solid interface," Langmuir **8**, 3033-3037 (1992).

Denn, M. M., "Extrusion instabilities and wall slip," Annu. Rev. Fluid Mech. **33**, 265-287 (2001).

Doi, M., "Explanation for the 3.4-power law for viscosity of polymeric liquids on the basis of the tube model," J. Polym. Sci., Polym. Phys. Ed. **21**, 667-684 (1983).

Doi, M. and S. F. Edwards, "Dynamcis of concentrated polymer systems. Part 1. Brownian motion in the equilibrium state," J. Chem. Soc. , Faraday Trans. 2 **74**, 1789-1801 (1978a).

Doi, M. and S. F. Edwards, "Dynamcis of concentrated polymer systems. Part 2. Molecular motion under flow," J. Chem. Soc. , Faraday Trans. 2 **74**, 1802-1817 (1978b).

Doi, M. and S. F. Edwards, "Dynamcis of concentrated polymer systems. Part 3. The constitutive equation," J. Chem. Soc. , Faraday Trans. 2 **74**, 1818-1832 (1978c).

Doi, M. and S. F. Edwards, "Dynamcis of concentrated polymer systems. Part 4. Rheological properties," J. Chem. Soc. , Faraday Trans. 2 **75**, 38-54 (1979).

Doi, M. and S. F. Edwards. *The theory of polymer dynamics*.(clarendon press oxford,1986)

Durliat, E., H. Hervet and L. Leger, "Influence of grafting density on wall slip of a polymer melt on a polymer brush," Europhys. Lett. **38**, 383-388 (1997).

Ferry, J. D. *Viscoelastic properties of polymers*.(John Wiley & Sons,New York,1980)

Fetters, L., D. J. Lohse, D. Richter, T. A. Witten and A. Zirkel, "Connection between polymer molecular weight, density, chain dimensions, and melt viscoelastic properties," Mcromolecules **27**, 4639-4647 (1994).

Flory, P. J. *Statistical mechanics of chain molecules*.(Interscience,New York,1969)

Hua, C. C. and J. D. Schieber, "Segment connectivity, chain-length breathing, segmental stretch, and constraint release in repation models. I. Theory and single-step strain predictions," Journal of chemical physics **109**, 10018-10027 (1998a).

Hua, C. C. and J. D. Schieber, "Segment connectivity, chain-length breathing, segmental stretch, and constraint release in repation models. Ii. Double-step strain predictions," Journal of chemical physics **109**, 10028-10032 (1998b).

Hua, C. C. and J. D. Schieber, "Segment connectivity, chain-length breathing, segmental stretch, and constraint release in repation models. Iii. Shear flows," J. Rheolo. **43**, 701-717 (1999).

Ianniruberto, G. and G. Marrucci, "On compatibility of the cox-merz rule with the model of doi and edwards," J. Non-Newtonian Fluid Mech. **65**, 241-246 (1996).

Inn, Y. W., M. M. Denn and K. F. Wissbrun, "Effect of edge fracture on constant torque rheometry of entangled polymer solutions," Macromolecules **38**, 9385-9388 (2005).

Joshi, Y. M. and A. K. Lele, "Dynamics of end-tethered chains a high surface coverage," J. Rheol. **46**, 427-453 (2002).

Joshi, Y. M., A. K. Lele and R. A. Mashelkar, "Molecular model for wall slip: Role of convective constaint release," Mcromolecules **34**, 3412-3420 (2001).

Kahvand, H. (1995). Strain coupling effects in polymer rheology. chemical engineering. Chicago, Illinois Institute of Techology.

Leger, L., H. Hervet, P. Auroy, E. Boucher and G. Massey, "The reptation model: Tests through diffusion measurements in linear polymer melts." *Rheology for polymer melt processing*. J.-M. P. a. J.-F. Agassant, Elsevier Science B. V.**,** 1-16(1996).

Likhtman, A. E. and R. S. Graham, "Simple constitutive equation for linear polymer melts derived from molecular theory: Rolie-poly model," J. Non-Newtonian Fluid Mech. **14**, 1-12 (2003).

Marrucci, G. and G. Ianniruberto, "Interchain pressure effect in extensional flows of entangled polymer melts," Macromolecules **37**, 3934-3942 (2004).

McLeish, T. C. B., "Tube theory of entangled polymer dynamics," Adv. Physics **51**, 1379-1527 (2002).

Mead, D. W., R. G. Larson and M. Doi, "A molecular theory for fast flows of entangled polymers," Macromolecules **31**, 7895-7914 (1998).

Mhetar, V. and L. A. Archer, "Slip in entangled polymer melts. 1. General features," Mcromolecules **31**, 8607-8616 (1998a).

Mhetar, V. and L. A. Archer, "Slip in entangled polymer melts. 2. Effect of surface treatment," Mcromolecules **31**, 8617-8622 (1998b).

Oberhauser, J. P., K. Pham and L. G. Leal (2004). Epaps document for the ariticle entitled "rheo-optical studies of the response of entangled polymer solutions to step changes in shear rate.

Ottinger, H. C. *Stochastic processes in polymeric fluids*.(Springer,Berlin,1996)

Pattamaprom, P. and R. L. Larson, "Constraint release effects in monodispers and bidisperse polystyrenes in fast transient shearing flows," Macromolecules **34**, 5229-5237 (2001).

Pearson, D., E. Herbolzheimer, N. Grizzuti and G. Marrucci, "Transient behavior of entangled polymers at high shear rates," Journal of polymer Science: Part B: Polymer Physics **29**, 1589-1597 (1991).

Ramamurthy, A. V., "Wall slip in viscous fluids and influence of materials of construction," J. Rheol. **30**, 337-357 (1986).

Rubinstein, M. and R. H. Colby. *Polymer physics*.(Oxford Univ. Press,Oxford,2003)

Stepanyan, R., J. J. M. Slot, J. Molenaar and M. Tchesnokov, "A slimple constitutive model for a polymer flow near a polymer-grafted wall," J. Rheol. **49**, 1129-1151 (2005).

Van Kampen, N. G. *Stochastic processes in physics and chemistry*.(North-Holland,Amsterdam,1992)

Venerus, D. C. and H. Kahvand, "Doi-edwards theory evaluation in double-step strain flows," J. Polym. Sci., Polym. Phys. Ed. **32**, 1531-1542 (1994).

Venerus, D. C. and R. Nair, "Stress relaxation dynamics of an entangled polystyrene solution following step strain flow," J. Rheology **50**, 59-75 (2006).

Volkenstein, M. V. *Configurational statistics of polymeric chains*.(Interscience,New York,1963)

Wise, G. M., M. M. Denn, A. T. Bell, J. W. Mays, K. Hong and H. Iatrou, "Surface mobility and slip of polybutadiene melts in shear flow," J. Rheol. **44**, 549 - 567 (2000).

Xu, F., M. M. Denn and J. D. Schieber, "A full-chain stochastic tube model for entangled melts and solutions of linear polymers," J. Rheol. **50**, 477-494 (2006).